NTNU
Norwegian University of
Science and Technology

Multiferroic, Magnetoelectric Nanoparticles

Lanthanum-substituted Bismuth Ferrite

Oddmund Hatling

Nanotechnology
Submission date: June 2011
Supervisor: Tor Grande, IMTE
Co-supervisor: Mari-Ann Einarsrud, IMTE
Sverre M. Selbach, IMTE

Norwegian University of Science and Technology
Department of Materials Science and Engineering

Declaration of independent work

I hereby declare that the work in this project has been performed independently and in accordance with the examination regulations of Norwegian University of Science and Technology (NTNU).

Oddmund Hatling

Acknowledgments

This work has been carried out at the Inorganic Materials and Ceramic Research Group, the Department of Materials Science and Engineering (DMSE), the Norwegian University of Science and Technology, NTNU, during the period January 2011 to June 2011.

There are many people I would like to thank for helping me with this project. I would first of all like to thank my advisor Professor Tor Grande and co-advisor Professor Mari-Ann Einarsrud for their many helpful advices throughout the year, and for being so easygoing. I would also like to thank my co-advisor Dr. Sverre Magnus Selbach for his numerous and detailed answers to my many questions. His doctoral thesis on $BiFeO_3$ have been worn out due to my many readings and a great portion of my understanding of the theory behind my research have been based on his comprehensive study. Next I would like to thank Dag Håkon Haneberg for his cooperation on the synthesis of the powder in which my work is based on, as well as his contribution to a lot of the comparative data presented here. Also, the rest of my work group, Professor Kjell Wiik, Astri Bjørnetun Haugen and Jon Strand have all participated with their comments on our weekly meetings.

I would like to thank Dr. Julian Tolchard for his help and advice on related and unrelated XRD questions and for being available at highly inappropriate times. Also, Sophie Weber deserves thanks for her quick and excellent thermal analysis. In closure I would like to thank all my classmates for being there for me when the night pushed on, and for making late night studies that much more interesting and fun.

Oddmund Hatling

Trondheim, 16th June 2011

Abstract

In this report, 10 at% lanthanum was introduced to the perovskite structure of bismuth ferrite at the expense of bismuth through a modified Pechini wet chemical method. Green body powders were calcined at several temperatures, and the lattice parameters for each size were found by Rietveld refinement of X-ray powder diffraction data. The parameters displayed strong size-dependent properties, and the rhombohedral distortion from the cubic structure was reduced by decreased particle size. With decreasing crystallite size, the Néel temperature decreased and the cooperative cationic displacement (s - t) showed size dependence at crystallite sizes below 30 nm. A size-dependency was also observed in the Curie temperature.

Contents

1 Introduction

1.1 Background

As society evolves, the need for new technology increases more rapidly than ever. Information technology is one of the cornerstones of this evolution, having seen an exponential improvement during the last half century. In recent years the need for ever decreasing sizes of transistors and other necessary components has intensified the focus of other ways of increasing computer performance without purely reducing structural dimensions. It is the process of reading, writing and storing data more efficiently that has fueled this attention.

One different way of meeting this challenge has been by using multiferroics instead of single-ferroic materials in the process. Multiferroic materials posses two or more of the main ferroic orders [1]: ferromagnetism, ferroelectricity and ferroelasticity, the two former being the most important. Although current technologies incorporate both ferro-electric and -magnetic materials and have been for a long time, no known materials display these properties at *room temperature* [2].

Perovskite and related compounds are widely investigated because of their multiferroic, photocatalytic and magnetic properties which are useful for applications in thin-film capacitors, nonvolatile memory, nonlinear optics and photoelectrochemical cells [3]. One of the most promising multiferroic material is the perovskite bismuth ferrite ($BiFeO_3$), as it shows the coexistence of both ferroelectricity and antimagnetic order. The ferroelectric Curie temperature T_C has been measured at 850°C while the antiferromagnetic Néel temperature T_N at 370°C. Bringing these two ordering temperatures down towards room temperature as well as closer together would enhance the coupling effect seen in other compounds of the same nature [4]. As the synthesis of perovskites like $BiFeO_3$ turned from thin-film, where epitaxial strain influenced the observed properties, towards a wet chemical synthesis with nanoparticles as a product, a finite crystallite size was observed [5, 6, 7, 8]. One effect of this was the relative displacement of the cations, a crystallographic measure of polarization, showing a significant value at reduced sizes, causing the antiferromagnetic order temperature T_N to drop. This is promising regarding the possibility of making small nanostructures with sufficient polarization for technological applications [5].

The nature of the rhombohedrally distorted perovskite $BiFeO_3$ reveals a superimposed incommensurate cycloid spin structure resulting in a net magnetization averaging to zero [9]. Another consequence of the cycloidal spin structure is that it inhibits the observation of a linear magnetoelectric effect, i.e. of the linear dependence of the induced electric polarization on the magnetic field [10]. In later years doping of $BiFeO_3$ by different cations has attained much focus due to the change in both the structure and multiferroic properties, much of it caused by the destruction of the cycloid spin structure. Doping with neodymium (Nd) [11], strontium (Sr) [12], manganese (Mn) [12, 13], and lanthanum (La) [3, 14, 15, 16] have been studied with different concentrations producing different, and often conflicting results.

It has been shown that by introducing lanthanum in $BiFeO_3$, one is able to maintain a stable structure while decreasing both the unit cell distortion and ferroelectric Curie temperature [2]. An early problem was the uncertain limit of dopant concentration in which the ferroelectric $R3c$ structure would change. A limit around 10 at% lan-

thanum was established, but further investigation on the size-dependency of the lattice parameters is needed to achieve a complete picture of happens in with the multiferroic properties of $Bi_{0.9}La_{0.1}FeO_3$.

1.2 Applications

The ongoing search for a better way to control the phenomena of multiferroicity and the great interest in multiferroic materials is attributed to the exciting and potentially groundbreaking impact this can have on several technology aspects. Especially the ability to maintain magnetization and a dielectric polarization which can be modulated and activated by an electric field and a magnetic field, respectively, makes multiferroic materials potential in several different applications [17]. One possible way of using multiferroics is shown in figure 1.1 where a binary information storage includes both the ferro-electric and -magnetic properties of the material. Its magnetic spins can be dictated by applying a voltage across the multiferroic ferroelectric-antiferromagnetic layer (FE-AFM; green). Applying a voltage directly changes the magnetization of the bottom ferromagnetic layer (blue) as this is coupled to these spins. A hysteric response curve can be attained by changing the magnetic configuration in the trilayer from parallel to antiparallel. In this way magnetoelectric random access memories (MERAMs) would have a drastically reduced energy requirement due to the use of voltage rather than currents. As of date, the best candidate for this use has been $BiFeO_3$, either as an element in a more complex MERAM design structure or as a stand-alone component [18].

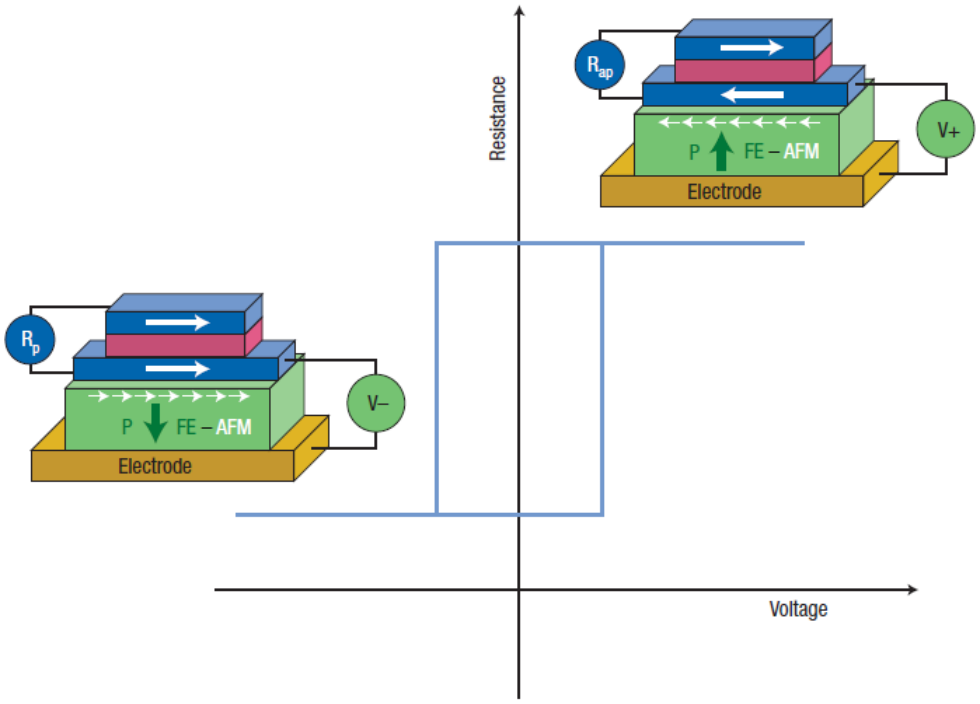

Figure 1.1: Sketch of a possible MERAM element, The binary information is stored by the magnetization direction of the bottom ferromagnetic layer (blue), read by the resistance of the magnetic trilayer (R_P when the magnetizations of the two ferromagnetic layers are parallel), and written by applying a voltage across the multiferroic ferroelectric– antiferromagnetic layer (FE -AFM; green). If the magnetization of the bottom ferromagnetic layer is coupled to the spins in the multiferroic (small white arrows) and if the magnetoelectric coupling is strong enough, reversing the ferroelectric polarization P in the multiferroic changes the magnetic configuration in the trilayer from parallel to antiparallel, and the resistance from R_P to antiparallel (R_{AP}). A hysteretic dependence of the device resistance with voltage is achieved (blue curve) [17]

1.3 Aim of work

The aim of this work is to study finite size effects in $BiFeO_3$ with 10 at% lanthanum substituted for bismuth, as phase pure $BiFeO_3$ is one of the very few known single phase room-temperature multiferroic material. The modified Pechini method will be used to synthesize nanocrystalline $Bi_{0.9}La_{0.1}FeO_3$ and perform calcination at temperatures from 400°C to 850°C to achieve a wide range of crystallite sizes. An important part of this work will be the study of how the unit cell parameters change as a function of crystallite size, and see if these changes also are visible from Curie and Néel temperature measurements.

2 Theory

2.1 Sol-gel synthesis

The sol-gel process is a widely used wet-chemical synthesis route within the fields of ceramic engineering and material science [19, 20, 21]. The process has its name from the starting chemical solution (*sol*) that acts as a precursor to form an integrated network (*gel*) of network polymers or discrete particles through different forms of hydrolysis and polycondensation reactions. Numerous solid colloidal particles within the liquid stabilizes the suspension, and it requires that these particles are large enough for further growth. The formation of colloids or polymeric gels are lead by the precursor reactions, and this growth continues until the particles in the liquid are completely unified. The gel point is defined at this temperature (or time) in which the last bond is formed to complete this giant molecule. Now, the solution has gone from a liquid state to a state in which a continuous liquid phase is enclosed by a continuous solid skeleton. Since there is still a sol within the gel network, this process goes on and those polymers or smaller particles continue to attach themselves to the network until a complete gelation of the sol precursor is done.

A drying process is needed to remove the remaining liquid (solvent), and during this heat treatment both shrinkage and densification occurs. This is due to the bond attraction or formation between particles causing expulsion of the liquid from the pores due to the contraction of the network. The conditions of this drying process are important factors for the final morphology of the gel. Performing this process at ambient temperature and pressure, the solvent evaporates to the air resulting in either a ambigel or a xerogel, depending on the solvent used. If this process is done under supercritical conditions (i.e. an autoclave) the interface between vapor and liquid is non-existing, this reducing the shrinkage of the gel due to the zero capillary pressure. This gel is mostly air with a solid volume fraction of as low as $\sim$1% and is called an aerogel.

2.1.1 Modified Pechini synthesis

Since a multicomponent oxide most often consist of ions of varying solubility, a way of trapping the different ions of the various salts is needed [19]. By dissolving hydrous oxides or alkoxides together with a polyhydroxy alcohol and a chelating agent, Pechini [22] patented a method for making powders consisting of Ti, Nb or Zr. This method resulted in nanosized particles due to the solution undergoing a polyesterification leading to a viscous resin, at temperatures relatively low compared to other synthesis method such as solid-state. Starting from zirconium oxychloride, Lin *et al.* [23] prepared ZrO_2 nanocrystals of various size via the Pechini method. The grain growth effects which occurred during calcination is shown in figure 2.1. Shown to the left is powder prepared by the Pechini method at 500°C with aggregated nanoparticles of approximately 80 nm in size, while the right shows powder treated at 1000°C in conventional solid-state synthesis being completely sintered together.

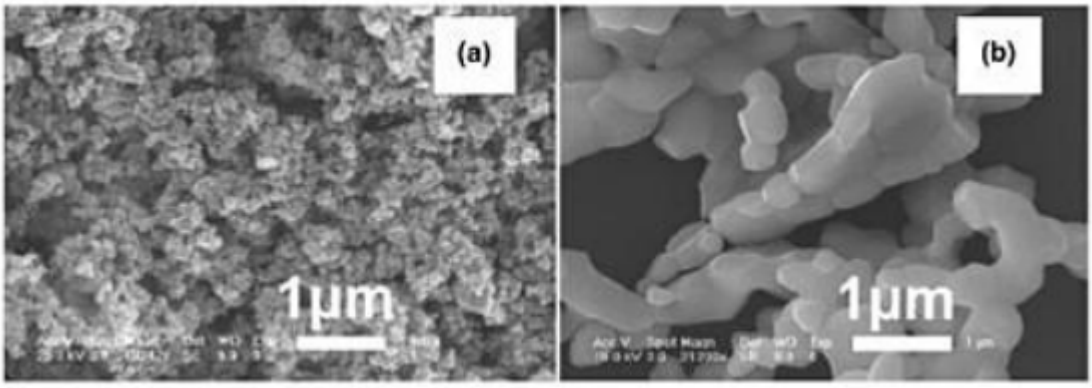

Figure 2.1: Scanning electron microscopy image illustrating the effect of the calcining temperature of nanopowders. (a) Zirconia nanoparticles obtained from Pechini method at 500°C, (b) the same particles transformed into large micrograins after annealing at 1000°C [23].

By adjusting the calcining temperature one is able to control the size of the particles or crystallites in the calcined powder. A powder calcined at a lower temperature will consist of particles smaller than those calcined at a higher temperature. Selbach [2] measured the crystallite sizes of $BiFeO_3$ powder prepared by modified Pechini synthesis with different carboxylic acid with or without ethylene glycol (EG) calcined at different temperatures, and found a strong dependence between size and temperature (figure 2.2a).

Hatling [24] observed a similar dependence in $Bi_{0.9}La_{0.1}FeO_3$ prepared by the same method using DL-tartaric acid and ethylene glycol as complexing and polymerizing agent, respectively (figure 2.2b). Although the results on $Bi_{0.9}La_{0.1}FeO_3$ are in a smaller size range than that of $BiFeO_3$, it is clear that temperature plays a crucial role in the growth of the crystallites.

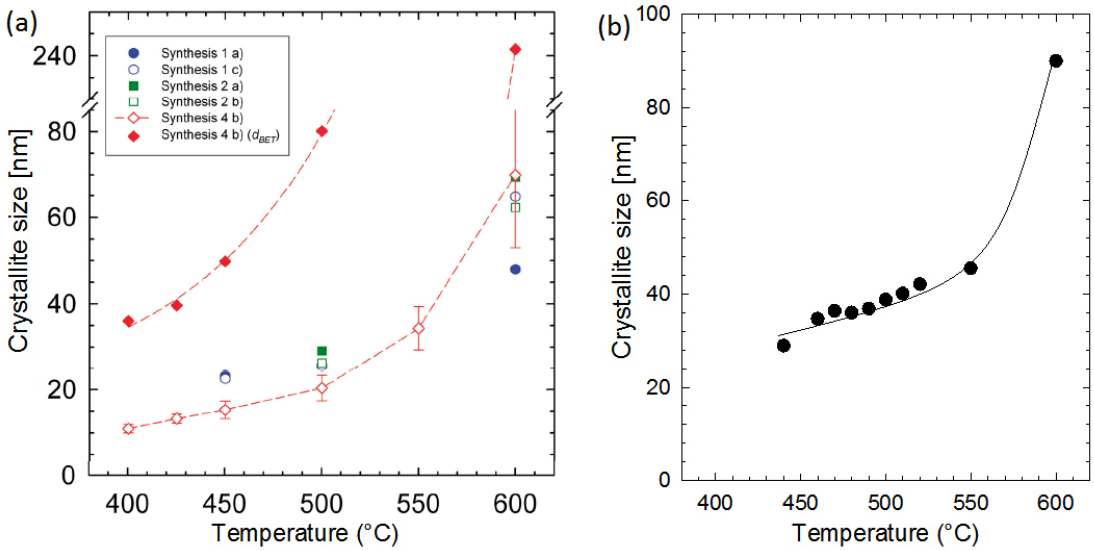

Figure 2.2: Size of (a)$BiFeO_3$ and (b) $Bi_{0.9}La_{0.1}FeO_3$ crystallites prepared by modified Pechini method as a function of calcination temperatures. The legends in (a) indicates the different synthesis routes, details in reference [2] and [24]. Lines are guides for the eye.

2.2 Crystal structure

2.2.1 Perovskite

The chemical formula for perovskite is represented by ABX_3, where A and B are cations and X usually oxygen [25]. The ideal perovskite structure is shown in figure 2.3. As fractional coordinates the A cation has $\frac{1}{2},\frac{1}{2},\frac{1}{2}$, B is in the origin (0,0,0) and the oxygen has $\frac{1}{2}$,0,0; 0,$\frac{1}{2}$,0; 0,0,$\frac{1}{2}$ (the structure can also be drawn with the A cation in the origin). From the figure the B site is in octahedral coordination with the neighboring oxygen anions, resulting in BO_6 octahedra forming a network running throughout the entire crystal. The A site has a coordinate number of 12, that is the number of neighboring atoms, all being oxygen.

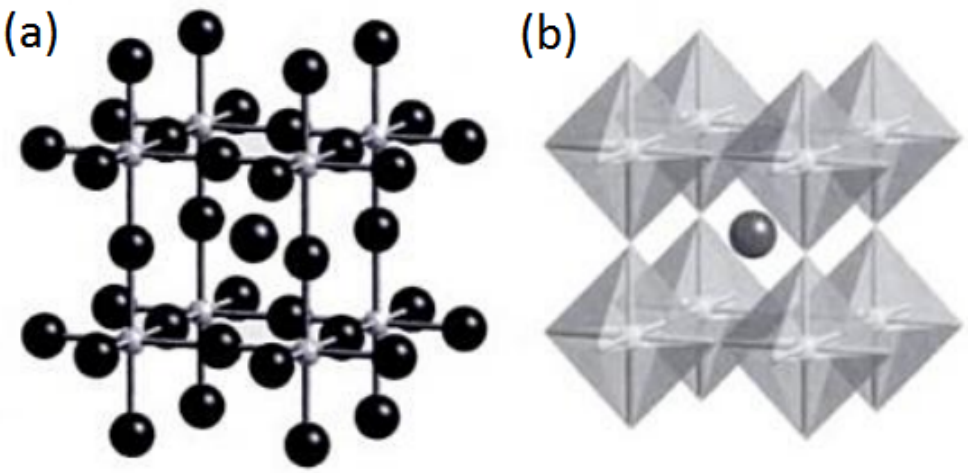

Figure 2.3: Ideal perovskite structure; (a) as atoms with bonds, (b) as a network of corner-linked octahedra [26].

A structural distortion is found in many perovskites and give rise to the important geometric and thermodynamic stability of the perovskite structure. This is mainly attributed to the size of the A and B cation. Treating the atoms in the structure as hard spheres, the bond lenghts in a cubic perovskite structure are related to the unit cell parameter, a, by

$$a = 2(r_B + r_O) = \sqrt{2}(r_A + r_O)$$

where r is the ionic radii and the subscript denotes the cation. This can be quantified by the Goldschmidt [27] tolerance factor, t:

$$t = \frac{(r_A + r_O)}{\sqrt{2}(r_B + r_O)} \tag{2.1}$$

Table 2.1 lists different compounds, the tolerance factor of the structures and properties related to them.

Table 2.1: Tolerance factor of some compounds and their structural properties [24, 25].

Tolerance factor (t)	Properties	Compound
< 0.85	Not stable perovskite (ex. hcp)	$LiNbO_3$, $FeTiO_3$
0.85 - 0.9	A cation is too small, distorted perovskite	$GdFeO_3$
0.9 - 1.0	Cubic perovskite	$BiFeO_3$, $CaTiO_3$
1.0 - 1.06	Stable perovskite, B cation slightly too small	$BaTiO_3$
$1.06 <$	Not stable perovskite (ex. tetrahedral Si)	$BaSiO_3$

As the table show, the tolerance factor is directly influencing the structural properties of the given compound. A cubic perovskite forms with t in the range $0.9 < t < 1.0$, it is here we find $BiFeO_3$. A slightly greater t distorts the structure but it is basically a perovskite, as in $BaTiO_3$. In a structure where t exceeds 1.06, the B ion demands a smaller site of lower coordination number and the structure changes completely, as in

$BaSiO_3$ which has tetrahedral Si. For smaller tolerance factors, $0.85 < t < 0.9$, it is the A cation that is too small for its site and a different kind of structural distortion occurs as in $GdFeO_3$. For t < 0.85, the distorted perovskite structures are no longer stable and the A cation requires a smaller site. Two examples are $FeTiO_3$ and $LiNbO_3$ whose structures are quite different from perovskite and both sets of cations occupying $\frac{2}{3}$ of the octahedral sites, making it basically a *hcp* structure.

Tolerance factors larger than unity are most commonly found in I-V and II-IV perovskites [2]. Within this range the distortion caused by the dissimilar size may enable favorable phenomena for certain applications. Also, slightly displaced B cations relatively to the ideal perovskite position results in distorted eccentric octahedra with important electrical properties [28].

2.2.2 Bismuth ferrite

Bismuth ferrite is probably the most well-studied Bi-based perovskite ferroelectric, both due to its multiferroic properties as well as the fact that it contains no lead, this making it more available for applications [29]. The $BiFeO_3$ structure is a rhombohedrally distorted perovskite with space group $R3c$, and can be viewed as a 3D network of corner-sharing FeO_6 octahedra with 12-coordinated Bi cations in voids between the octahedra (figur 2.4) with lattice parameters $a_r = 5.63$ Å, $\alpha_r = 59.35°$, or alternatively as a hexagonal structure with parameters $a_{hex} = 5.58$ Å and $c_{hex} = 13.87$ Å [5, 30, 31].

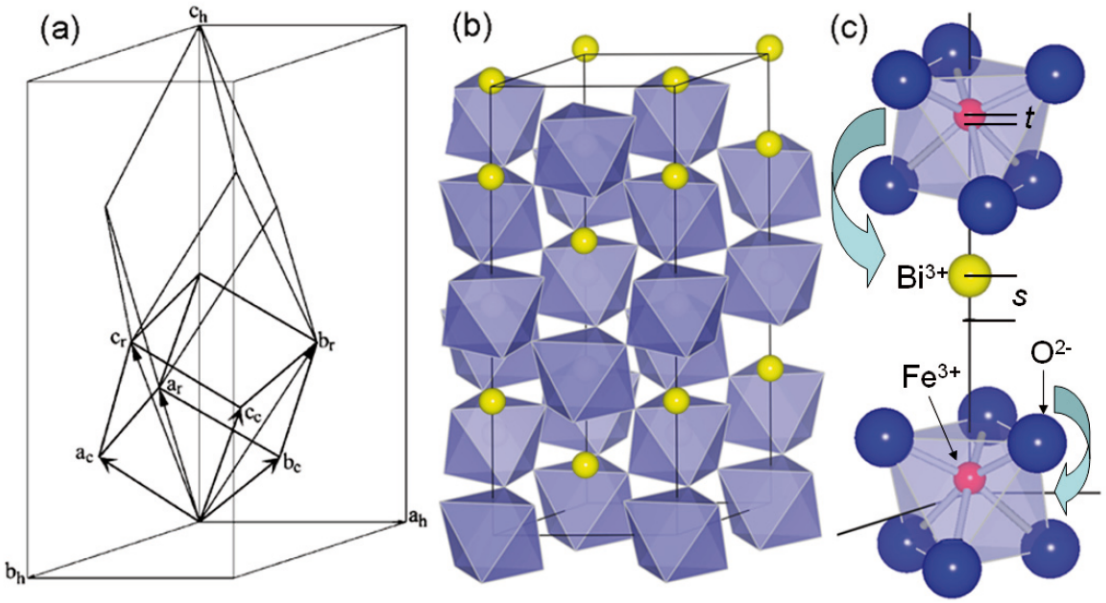

Figure 2.4: (a) Relation between pseudocubic, rhombohedral and hexagonal setting of the unit cell of $BiFeO_3$ with space group $R3c$. (b) Hexagonal unit cell of $BiFeO_3$, showing Bi^{3+} cations (yellow) and FeO_6 (blue). (c) Illustration of the atomic positions given in table 2.2, showing cationic displacement, s and t. The FeO_6 octahedra rotate antiparallel about the $[001]_{hex}$ axis [2].

As can be seen by figure 2.4, the normalized lattice parameters in this structure are given by $a_{norm} = a_c = \frac{a_{hex}}{\sqrt{2}}$ and $c_{norm} = c_c = \frac{c_{hex}}{\sqrt{12}}$. The ratio $\frac{c}{a}$ is important

when calculating the relative cubic structure, and thus also the chance for ferroelectric properties explained in chapter 2.3.1.

Table 2.2 shows the atomic positions of Bi^{3+}, Fe^{3+} and O^{2-} in the hexagonal setting of $R3c$ [32].

atom/pos	x	y	z
Bi^{3+}	0	0	$\frac{1}{4} + s = 0.30$
Fe^{3+}	0	0	$t = 0.02$
O^{2-}	$\frac{1}{6}$ - $2e$ - $2d = 0.23$	$\frac{1}{3}$ - $4d = 0.34$	$\frac{1}{12}$

Table 2.2: Atomic positions in the hexagonal setting of $BiFeO_3$ ($R3c$) [5, 32].

The unit cell is anchored in the z-direction by the oxygen position fixed at $\frac{1}{12}$ along the c-axis, as shown in figure 2.4c. The displacement of the cations from their ideal position, s for Bi and t for Fe, has shown to have a linear relation to the spontaneous polarization of some perovskites, as well as in $BiFeO_3$ [5].

A feature $BiFeO_3$ share, not only with its family of ferroelectric nanoparticles, but with all oxide nanoparticles, is unit cell expansion with decreasing particle size. This is attributed to surface layer relaxation and changes of the valence of ionicity of cations among others [33].

The pseudo-binary phase diagram [2] of the system Bi_2O_3–Fe_2O_3 in figure 2.5 contains three ternary phases at room temperature; sillenite ($Bi_{25}FeO_{39}$), the perovskite ($BiFeO_3$) and mullite ($Bi_2Fe_4O_9$). The formation of the sillenite and mullite phases is a challenge during ceramic and chemical routes to obtain $BiFeO_3$. From the figure it is clear that a deviation from the $BiFeO_3$ stoichiometry either way will produce these phases, and different phase transition temperatures occurs in these compositions.

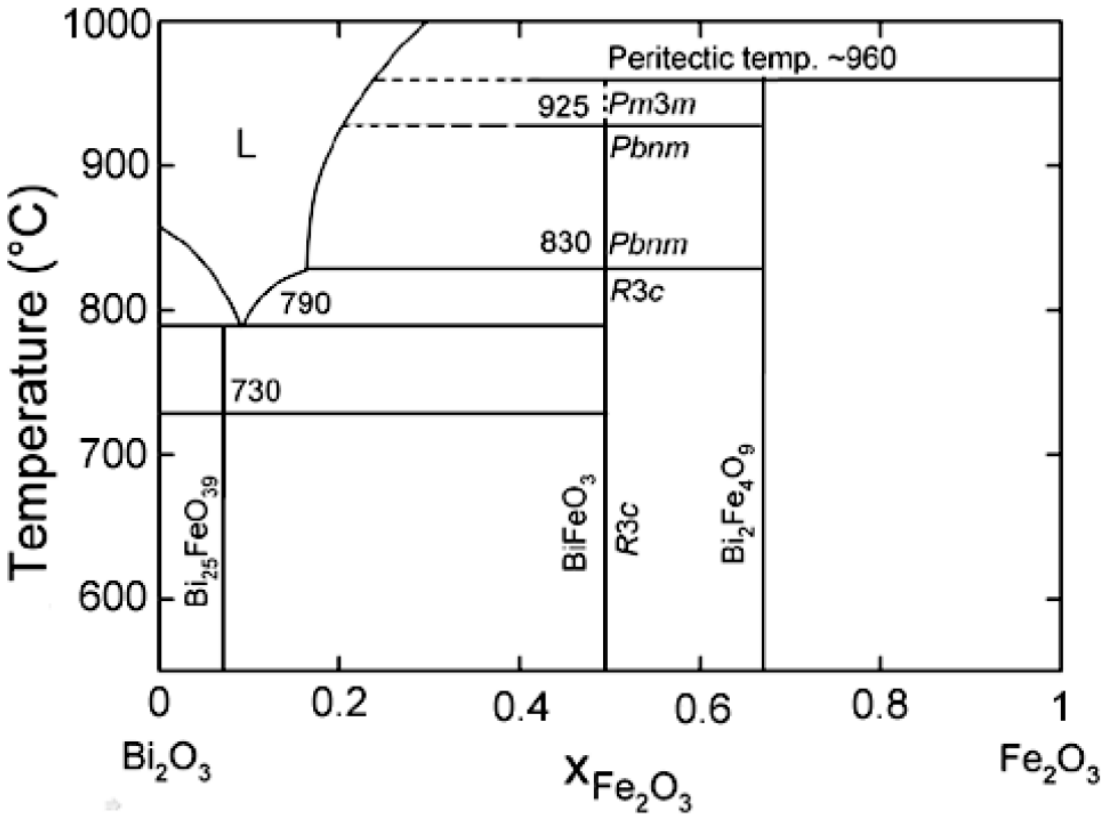

Figure 2.5: Binary phase diagram of the system Bi_2O_3–Fe_2O_3 [2]

2.2.2.1 Stability of $BiFeO_3$ There are debates about what is causing the secondary phases to occur, and there are contradicting reports of what temperature favors them. Selbach [2] and Carvalho *et al.* [34] used XRD (HTXRD in the former) to observe the chemical reaction of $BiFeO_3$ as

$$\frac{12}{49}Bi_2Fe_4O_9 + \frac{1}{49}Bi_{25}FeO_{39} = BiFeO_3 \tag{2.2}$$

with $Bi_2Fe_4O_9$ being mullite and $Bi_{25}FeO_{39}$ sillenite. Both authors saw an increase in the secondary phases at temperatures between 600°C and 850°C, indicating a metastable phase at this temperature. Popa *et al.* [35] observed the opposite by using XRD, Raman spectroscopy and SEM/TEM, as the secondary phases occurred at 350°C and disappeared at 600°C with only phase pure $BiFeO_3$ left.

Much of the available literature shows that the wet chemical synthesis of $BiFeO_3$ gives a more phase pure powder than that of the solid state synthesis [2, 36, 37]. The latter synthesis tends to contain minor secondary phases clearly detectable by XRD. This synthesis is done using the binary oxides Bi_2O_3 and Fe_2O_3, and deviation from the normal 1:1 stoichiometric ratio of Bi:Fe is caused by the low intrinsic solid solubility. Due to the low tolerance for vacancies in the cation sublattices, this implies that the nominal stoichiometry must be carefully controlled. However, numerous authors report these unwanted phases more or less appearing in wet chemical synthesis as well, both in undoped and doped $BiFeO_3$. Different authors attribute this to different reasons; either from the pH in which the sol is obtained or to which carboxylic acid used as complexing agent. In the former, Jiang *et al.* [38] increased pH in the precursor solution to reduce

the formation of mullite by adding aqueous ammonia, although they was not able to remove the mullite formation totally. Jiang *et al.* used citric acid as complexing agent, which was proposed by Ghosh *et al.* [36] to be the source of the unwanted phase. it was concluded that the impurities seen for citric acid and not for tartaric acid was caused by the dimeric nature of the citric $BiFeO_3$-complex not promoting the formation of Bi(III)-Fe(III) heteronuclear arrangement.

2.2.3 Lanthanum doping of $BiFeO_3$

As seen in chapter 2.2.1, the tolerance factor is crucial in maintaining the perovskite structure and care is to be considered when doping it. A way to induce "pressure" in a crystal is by chemical substitution of an ion for another of the same valence but different size, what is sometimes called "chemical pressure" [39]. The most common isovalent substitute in $BiFeO_3$ is La^{3+} for Bi^{3+}, which has almost the exact same ionic radii (1.16 Å and 1.17 Å, respectively [40]). As ferroelectric distortion in La-doped $BiFeO_3$ is observed, this has been attributed to the missing $6s^2$ lone-pair in the dopant rather than the direct difference in ionic size. Selected properties of the end members $BiFeO_3$ and $LaFeO_3$ are given in table 2.3. Depending on the amount of added La in exchange for Bi, the distortion along the polar c-axis changes due to La atoms substituting Bi atoms on the A cation site. A structural transformation from rhombohedral to orthorhombic is seen when approaching a certain at% La, and these values have been measured to vary from 0.05 to 0.125.

	$BiFeO_3$	$LaFeO_3$
Space group	$R3c$	$Pbnm$
$a_{norm.}$(Å)	3.984	3.929
$b_{norm.}$(Å)	(3.984)	3.935
$c_{norm.}$(Å)	4.004	3.927
Volume[a] (Å^3)	63.546	60.721
T_N (°C)	370	470

Table 2.3: Selected properties of $BiFeO_3$ and $LaFeO_3$ [2].

By introducing 5 - 25 at% La in $BiFeO_3$, Selbach [2] showed this structural evolution by observing the change in peak shape and splitting in XRD patterns (figure 2.6a). The reduced splitting of the $(104)_{hex}$ reflection points to a less distorted crystal structure with increased La content. Figure 2.6b shows the mole fraction of each phase based on Rietveld refinement of the XRD data, and clearly defines the region in which the composition goes changes from a single phase (rhombohedral $R3c$) to a two-phased region (orthorhombic Pbnm + $R3c$). This is when the nominal La content is below 0.125. He also found that La substitution up to 10 at% introduced structural disorder and lattice strain, but did not change the space group of $BiFeO_3$. Figure 2.6c from the same work clearly shows a region where the structure shows no signs of the secondary phases, indicating a stable perovskite within this interval.

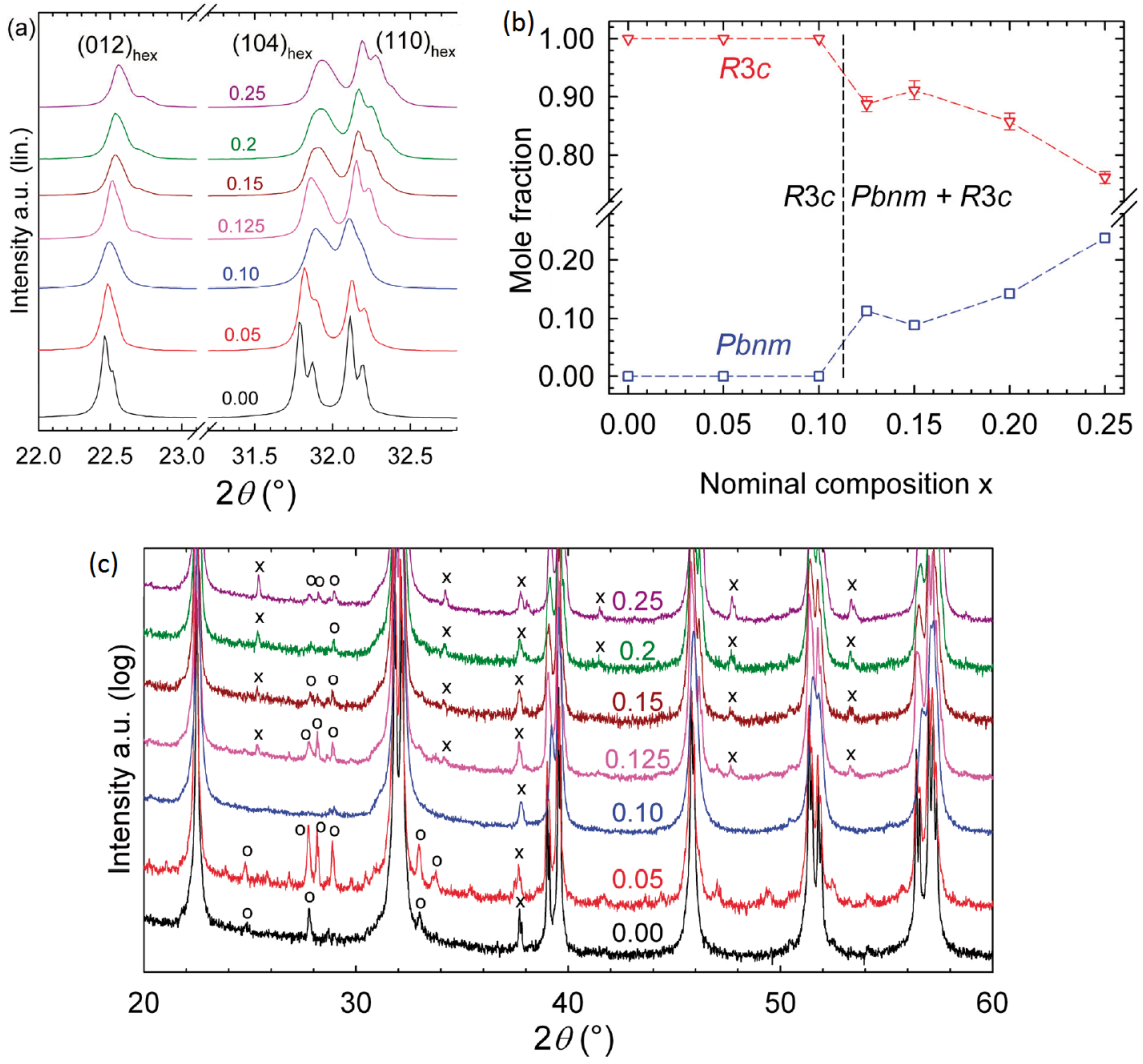

Figure 2.6: (a) Structural evolution shown by peak shape and splitting of La-substituted $BiFeO_3$. (b) Proposed phase composition as a function of nominal La content x. (c) Logarithmic scale highlighting the low-intensity reflections. Reflections marked x or o are due to trace amounts of $Bi_{25}FeO_{39}$ and $Bi_2Fe_4O_9$, respectively [2].

Hatling [24] used the modified Pechini method to see what effect the crystallite size of the La-doped powder had on the the different properties of the structure. Only minute trace amounts of the secondary phases were detected over a range of crystallites sizes, and these were undetectable at bulk. This indicates that the mobility of atoms in the structure are sensitive to the thermal energy from the different calcining temperatures. Figure 2.7 shows the evolution of the peaks from amorphous powder to bulk for $Bi_{0.9}La_{0.1}FeO_3$.

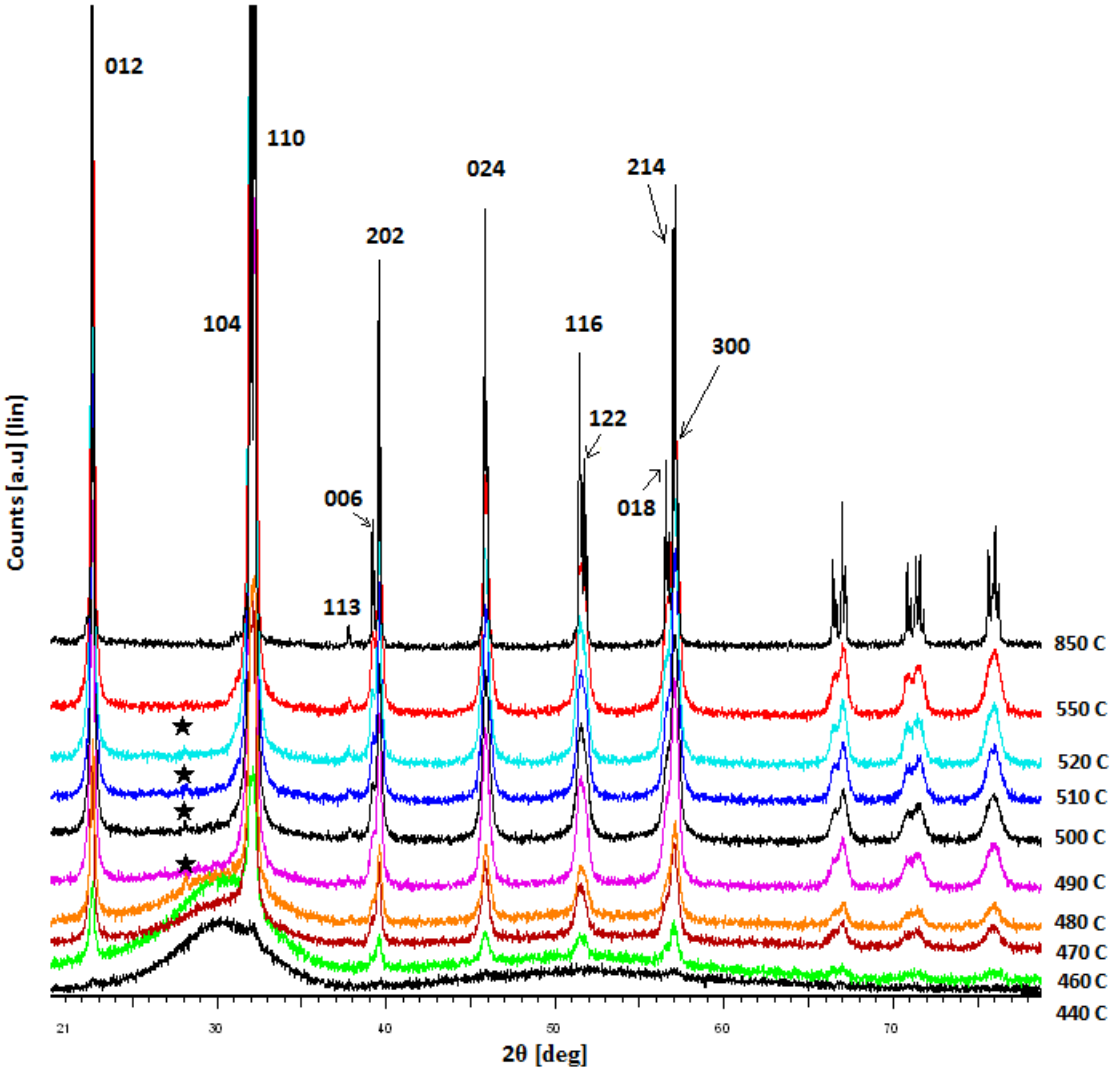

Figure 2.7: XRD patterns of $Bi_{0.9}La_{0.1}FeO_3$ with the Miller indices giving the {hkl} phases synthesized by the modified Pechini method from Hatling, temperatures are given to the right for each pattern [24]. The black star denote reflections from secondary phases.

The majority of reports on La-doped $BiFeO_3$ have focused on the multiferroic properties, while the structural research has been scarce. This has fueled a debate about what happens with the structure when lanthanum is introduced.

Simoes *et al.* [16] showed that lanthanum substitution reduced the strain behavior of $BiFeO_3$ films. From leakage current density values they noted that La^{3+} substitution for Bi^{3+} was an effective way to reduce bismuth vacancies accompanied by oxygen vacancies decreasing film conductivity.

Lin *et al.* [15] and Garcia *et al.* [3] found that the traces of mullite and sillenite was reduced by increased La doping. In the former work traces appearing in both undoped and 10 at% became undetectable at 15 at% La, while in the latter work the traces was undetectable already at 8 at% La. In an effort to explain the secondary phases appear in their XRD data for $BiFeO_3$ doped with 20 at% La using hydrothermal heat treatment of the green powder, Yan *et al.* [14] noticed that these peaks were due to

the Fe_2O_3 phase rather than $Bi_2Fe_4O_9$ phase. A reason for this was believed to be the nature of the hydrothermal synthesis which became more complicated than wet chemical synthesis upon using cation substitution. Using the solid state synthesis, in which Bi_2O_3, $Fe_2O_3$and La_2O_3powder are mixed to a slurry and dried, Das *et al.* [41] also observed this change in crystallinity happening at around 5 - 10 at% La, although the data from the XRD was not good enough to give a clear answer.

2.3 Ferroic ordering

2.3.1 Ferroelectricity

If a material showing a spontaneous electric polarization direction can be switched by applying a field, it is considered to be ferroelectric [42]. What distinguish ferroelectric materials from ordinary dielectrics are (a) their extremely large permittivities and (b) the possibility of retaining some residual electrical polarization after the applied voltage has been switched off [24]. The linear dependence between applied voltage and induced polarization shown in ordinary dielectrics does not hold. Instead, a hysteresis loop arises, showing properties like saturation polarization, P_S, at high field strength and a remnant polarization, P_R, which is the polarization retained as the voltage is subsequently reduced to zero (see figure 2.8). This effect disappears above a certain material dependent temperature called the Curie temperature, T_C. Due to the thermal motion which breaks down the common displacement and destroys the domain structure, the material becomes paraelectric (non-ferroelectric) above this point.

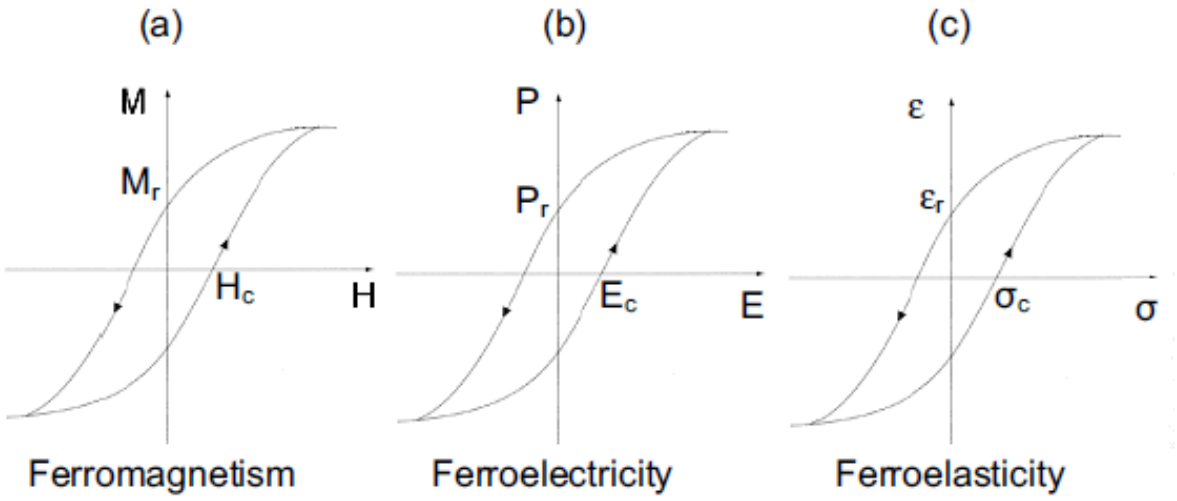

Figure 2.8: Hysteresis loops characteristic for: (a) ferromagnetism; (b) ferroelectricity; (c) ferroelasticity. The y-axis is the magnetization (M), electric polarization (P) and microscopic strain (ϵ), the x-axis is the magnetic field (H), electric field (E) and mechanical stress (σ), for (a), (b) and (c), respectively. The subscripts r and c means remnant and coercive [2].

The most studied and widely used ferroelectric today is the perovskite structure, undergoing a phase transition from the high temperature cubic structure to a spontaneously polarized phase below its T_C [25]. The electric dipole moment caused by the

structural shift in the A and/or B cations relative to the oxygen anions causes the spontaneous polarization to appear. If the adjacent dipoles are arranged antiparallel to each other antiferroelectricity is present, which is a related type of spontaneous polarization.

It would be impossible for ferroelectricity to exist in an entirely ionic bonded symmetric crystal structure. The dipole moment would be suppressed by the force rising from the short range repulsion between adjacent closed shell ions, forcing the structure to remain centrosymmetric and thus not ferroelectric. It is the balance between these short range repulsions and additional bonding considerations stabilizing the distortions that determines the absence or existence of ferroelectricity.

The Curie temperature in the prototype ferroelectrics $PbTiO_3$ and $BaTiO_3$ are 490°C and 123°C, respectively. By cooling these compounds through this temperature a transformation from the cubic high-temperature structure to a tetragonal, polar structure occurs, causing a displacement of the Ti^{4+} cation large enough to break symmetry and thus providing electric dipoles along the [001] direction [43, 44]. The substantially higher tetragonality (unit cell distortion, $\frac{c}{a}$), T_C and spontaneous polarization of $PbTiO_3$ compared to $BaTiO_3$ shows the importance of the $6s^2$ lone pair of Pb^{2+} as this takes part in the covalent bonding with O 2p orbitals.

The spontaneous polarization P_S of $BiFeO_3$ is parallel to $[001]_{hex}$-axis, and the displacement of Bi^{3+} caused by the stereochemically active $6s^2$ lone pair is the main source for this [45]. The covalent bonding between the $6s^2$ lone pair of Bi^{3+} and O^{2-} 2p orbitals has also been confirmed theoretical [46], as well as between Fe^{3+} and O^{2-}. This polarization is shown to be larger than those of $BaTiO_3$ and $PbTiO_3$ due to higher Curie temperature and more distorted crystal structure, the former being 820°C - 830°C for $BiFeO_3$ [47].

By introducing different rare earth dopants in the $BiFeO_3$ structure, Karimi *et al.* [48] measured both the T_C and the average tolerance factor, t, for each composition. They found that $BiFeO_3$ doped with equal or less than 10 at% RE favored the $R3c$ phase at room temperature. Figure 2.9 shows T_C as a function of t for $BiFeO_3$ doped with 10 at% lanthanum, neodymium, samarium and gadolinium, and as the tolerance factor decrease (with decreasing ionic radii, $r_{La^{3+}} > r_{Nd^{3+}} > r_{Sm^{3+}} > r_{Gd^{3+}}$), so does T_C.

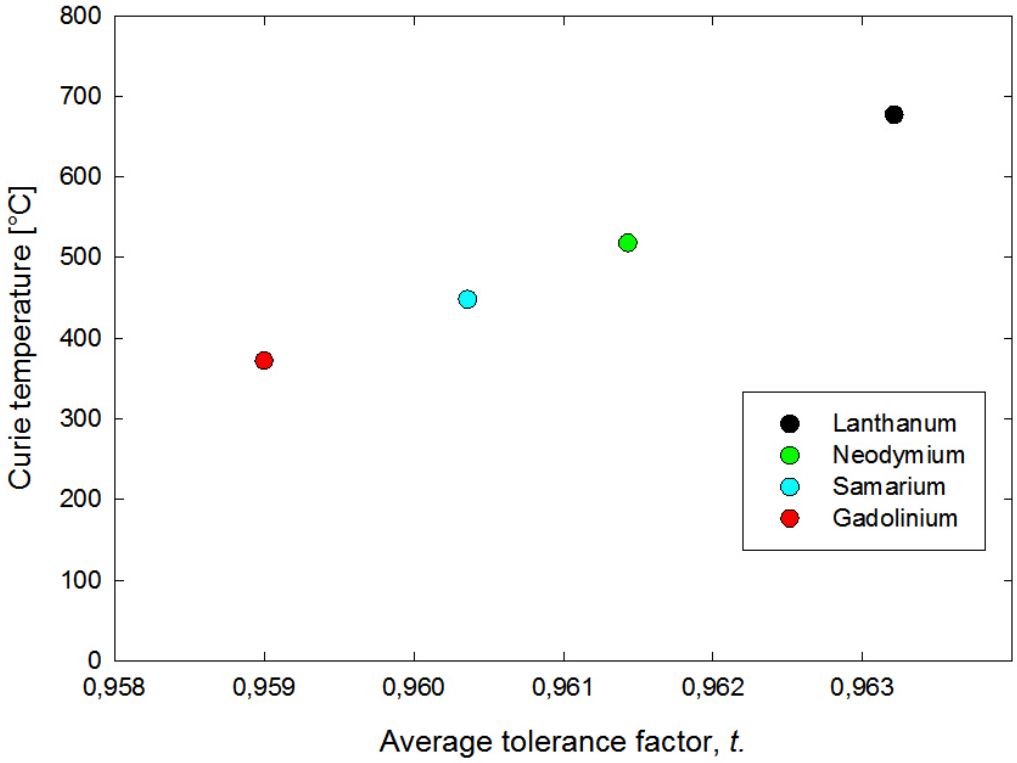

Figure 2.9: Curie temperature as a function of the average tolerance factor of $BiFeO_3$ substituted by four different rare-earth metals [48].

Table 2.4 shows T_C measured on both doped and undoped $BiFeO_3$. It is clear that the doping of $BiFeO_3$ with lanthanum reduces the temperature significantly in which the ferroelectric phase transition occurs, in good compliance with Karimi [48], while the synthesis route is shown to be less significant.

Dopant	Synthesis route	Measured T_C	Reference
Undoped	Modified Pechini	830°C	[5]
Lanthanum	Modified Pechini	680°C	[24]
Lanthanum	Solid state reaction	675°C	[2]
Lanthanum	Reaction with alcohol and spin coated	680°C	[49]
Samarium	Modified Pechini	459°C	[50]

Table 2.4: T_C of $BiFeO_3$ substituted by different rare-earth metals.

The substitution of Bi^{3+} for the larger La^{3+} ions would increase the tolerance factor, t, which might be an explanation for the reduction [51]. Compared to Bi^{3+}, La^{3+} does not possess a $6s^2$ lone pair believed to be imperative for stabilization of the polar, ferroelectric $R3c$ structure. The missing partial covalent bonding between La^{3+} and O^{2-} as well as the more basic nature of La^{3+} may lead to a reduction in the ferroelectric properties of $BiFeO_3$ by doping.

2.3.2 Magnetic properties

Ferromagnetism is the existence of a spontaneous magnetization which can be reversed by an opposite magnetic field, in the same way as electric polarization can be reversed by an electric field (figure 2.8). All materials in nature possess some form of diamagnetic response to an applied magnetic field [29]. However, there are several other magnetic phenomena present in some inorganic solids caused by unpaired electrons. Usually located on metal cations, these phenomena of magnetic behavior are mainly restricted to compounds of lanthanides and transition metals, most of which possess unpaired f and d electrons, respectively. The different effects for a schematic 1D crystal are shown in figure 2.10 [25]. Paramagnetism (a) is a state where the magnetic polarization is randomly oriented and with a positive magnetic susceptibility, meaning that the material is in a state where it is attracted to the magnetic field. Unlike ferromagnetism (b), where induced magnetic moment is retained in the absence of an externally applied magnetic field, and thermal motion causes the spins to become randomly oriented without it, reducing the total total magnetization to zero when the field is removed. In antiferromagnetism (c), the overall magnetic moment is zero due to neighboring spins pointing in opposite directions, whereas ferrimagnetism (d) occurs when neighboring spins are pointing in opposite directions but of unequal size, resulting in a net magnetic moment.

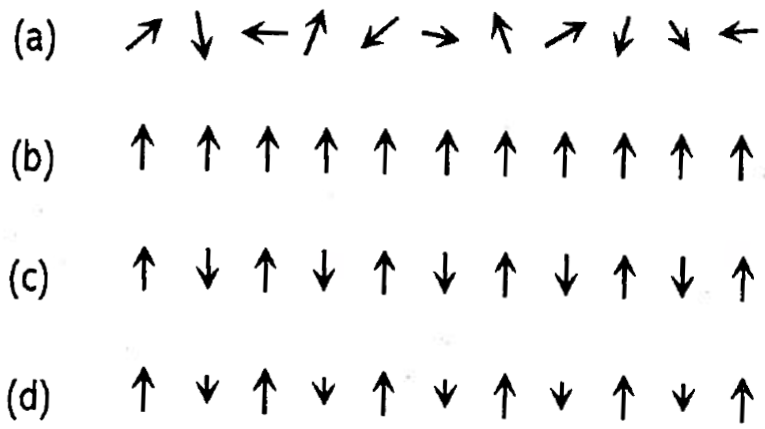

Figure 2.10: Schematic magnetic phenomena in a 1D crystal: (a) paramagnetism; (b) ferromagnetism; (c) antiferromagnetism; (d) ferrimagnetism [25].

As ferromagnets experience a phase transition from ferromagnetic to paramagnetic orientation above the Curie temperature T_C, antiferromagnets experience a phase transition from antiferromagnetic to paramagnetic above the Néel temperature T_N. This is caused by the magnetic susceptibility passing through a maximum, due to sublattices antiparallel to the magnetic field being most susceptible to reorientation by a field at T_N. $BiFeO_3$ is an antiferromagnet with G-type ordering [52], each Fe^{3+} with spin up is surrounded by six nearest neighbors with spin down. Perpendicular to the polar $[111]_{hex}$ axis is the easy plane of magnetization ($(001)_{hex}$), this can be visualized in figure 2.11. The reduction of the Fe-O-Fe angle from 180° caused by the tilting of the FeO_6 octahedra reduces the overlap of O 2p and Fe d orbitals. It is this tilting of the

sublattices to 154-155° that yields a weak ferromagnetic moment. This is however cancelled due to an average spiral modulation with periodicity of 62 nm, incommensurate with the crystal lattice [9].

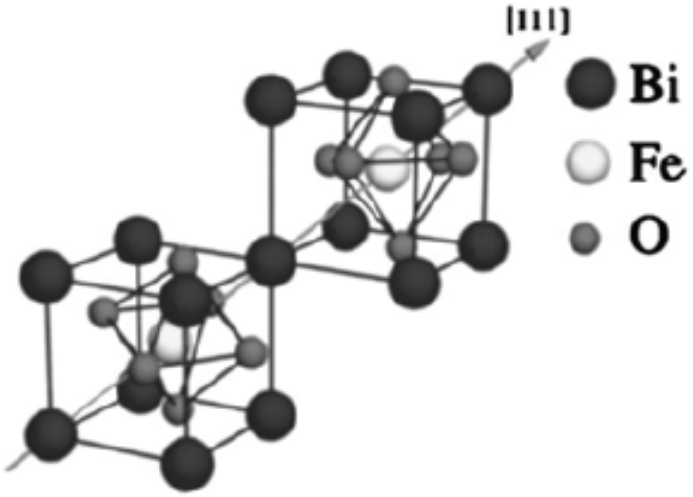

Figure 2.11: Structure of $R3c$ $BiFeO_3$. Shows the tilted FeO_6 octahedra giving rise to the total weak ferromagnetic moment which in turn is cancelled due to average spiral modulation [53].

As the Néel temperature for $LaFeO_3$ and $BiFeO_3$ are reported to be ∼470°C and ∼370°C, respectively [15, 54, 55], introducing lanthanum into the $BiFeO_3$ structure should increase T_N. Chen *et al.* [55] measured the Néel temperatures as a function of La-content in $BiFeO_3$ ceramics. Figure 2.12 shows the temperature increasing with increased dopant concentration. It is worth noting that this increase is small in dopant concentrations below 30 at% compared to higher concentrations. This is thought to be due to the structural phase transition observed for dopant concentrations above 30 at%. Lin *et al.* [15] explained this minute variation in the Néel temperature for structures with dopant concentrations below 30 at% as inherent to the nature of the dopant. They noted that though the La substitution-induced suppression or destruction of spin cycloid leads to the observation of a weak ferromagnetism, such behavior does not change the nature of the canting of the antiferromagnetic sublattices, resulting in the similarity of the temperature dependence of magnetization for various La dopant concentrations.

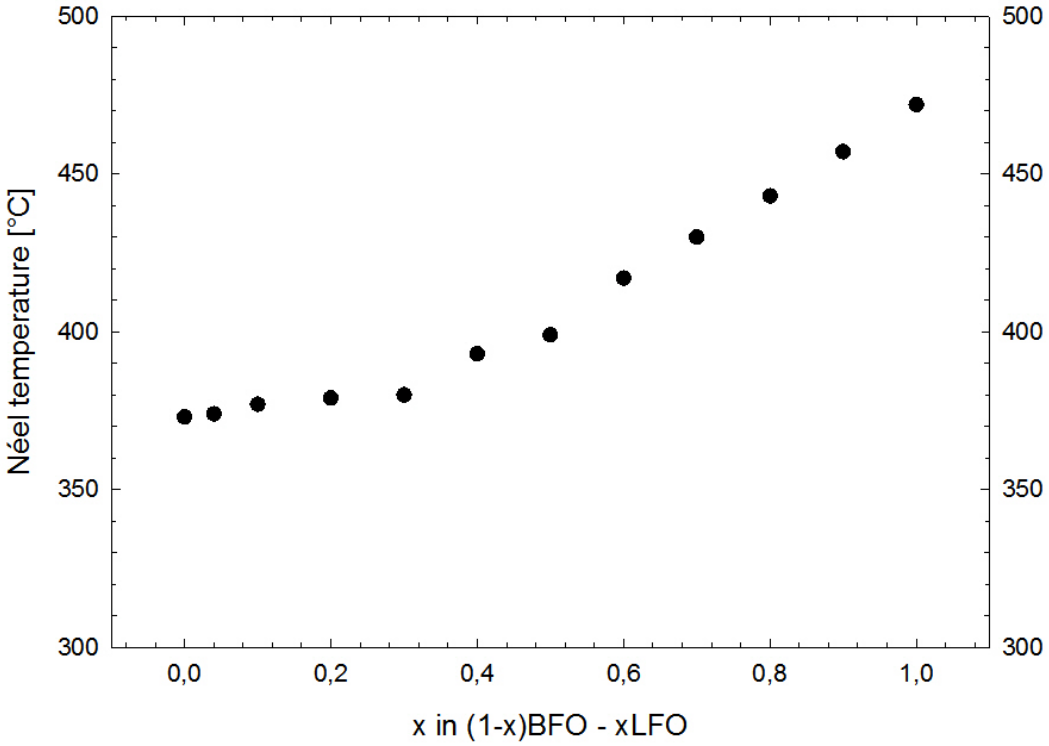

Figure 2.12: The phase boundaries of the antiferromagnetic–paramagnetic transition of $_{(1-x)}$BFO$-_{x}$LFOceramics [55].

Experiments measuring the Néel temperature in doped and undoped $BiFeO_3$ have been reported. Table 2.5 shows the Néel temperature of bulk-like $BiFeO_3$, both undoped and doped with rare earth metals. Compared to the results on undoped $BiFeO_3$, lanthanum is seen to have only sporadic influence on the antiferromagnetic to paramagnetic phase transition at bulk, being fixed around 360 - 380°C.

Dopant	Synthesis route	Measured T_N	Reference
Undoped	Modified Pechini	370°C	[5]
Undoped	Modified Pechini	384°C	[36]
Lanthanum	Modified Pechini	370°C	[15]
Lanthanum	Modified Pechini	378°C	[24]
Lanthanum	Solid state reaction	378°C	[2]
Lanthanum	Modified Pechini with autoclaves	364.2°C	[14]
Samarium	Modified Pechini	382°C	[50]

Table 2.5: T_N of $BiFeO_3$ substituted by different rare-earth metals.

2.3.3 Ferroelasticity

A material with ferroelastic properties show spontaneous phenomena related to its ferroic nature as the case is for ferromagnetism and ferroelectricity. For ferroelastic materials, this is a spontaneous strain occurring as a stress is applied to the material [56].

This stress induces a change from one phase to an equally stable phase either of different orientation or different structure. Due to the difficulties in observing ferroelasticity and ferromagnetism/ferroelectricity simultaneously, the relation between them has not been investigated to the same extent as that of the two latter. For this reason, the coexistence of magnetism and ferroelectricity is what most people mean by multiferroic properties in a material [4].

2.4 Multiferroic properties

Although the formal definition of a multiferroic material is under debate, it is often defined as materials which exhibit more than one primary ferroic order parameter simultaneously (in the same phase) [57, 58]. These primary ferroic parameters are ferroelectricity, ferromagnetism and ferroelasticity. The two former ferro-parameters have shown interesting coupling effects and the origins are fundamentally different [59]; ferroelectricity results from relative shifts of negative and positive ions that induce surface changes, while ferromagnetism is related to ordering of spins of electrons in incomplete ionic shells (concept shown in figure 2.13).

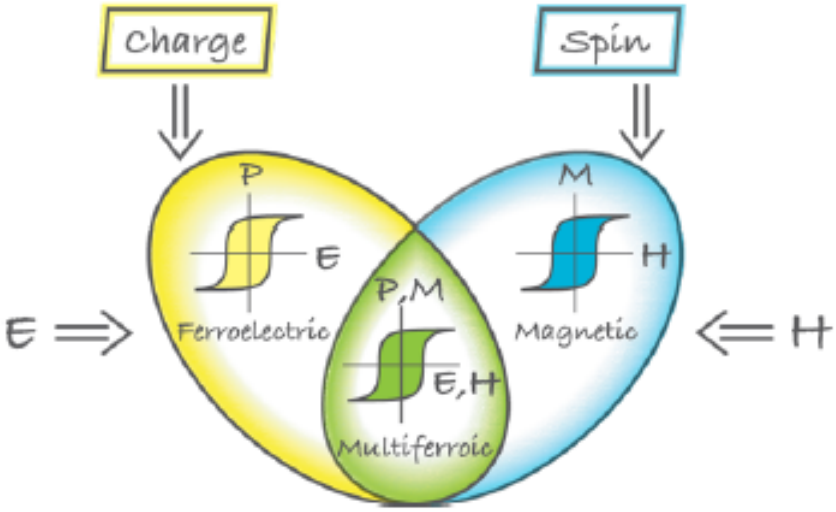

Figure 2.13: Multiferroics combine the properties of ferroelectrics and magnets. Usually the polarization from charge (yellow) and the magnetization from spins (blue) are separated, although similar in nature by the observed hysteresis loop [4].

There are two general groups of multiferroics, called type-I and type-II multiferroics. The former contains those materials in which magnetism and ferroelectricity have different sources and appear largely independently of one another, but still have some coupling between them. Ferroelectricity typically appears at higher temperatures than magnetism in these materials, and the spontaneous polarization P_S is often large. It is in this category $YMnO_3$ and $BiFeO_3$ belongs, with T_C at ~640°C and ~830°C and T_N -197°C and 370°C, respectively. The latter group of multiferroics contains materials where ferroelectricity is caused by magnetism, implying a strong coupling between the two (examples are $Ni_3V_2O_6$, $MnWO_4$ and $TbMnO_3$) [4].

There are many magnetic materials among perovskites, and also many ferroelectrics. But comparing these extensive compilations, each containing hundreds of tables, demonstrate that there seems to be a mutual exclusion of magnetism and ferroelectricity in perovskites; compounds showing both is very rare [58]. Whereas the former is largely caused by empty d shells in transition metal oxides due to the collective shift of anions and cations, the latter requires transition metal ions with partially filled d shells, as the spins of electrons occupying completely filled shells add to zero and do not participate in magnetic ordering. It is this conflict; one needs partially filled d shells while the other other wants them empty, that makes these two ordered states mutually exclusive.

Still, compounds such as $BiFeO_3$ and $BiMnO_3$, with magnetic Fe^{3+} and Mn^{3+} ions, are ferroelectric. This is due to the $6s^2$ lone pair electrons in bismuth, allowing the ion to move away from the centrosymmetric position relative to its oxygen surroundings [60]. These are type-I multiferroics with multiferroic properties associated with different ions making the coupling between them weak. With the former having a G-type antiferromagnetic ordered cycloid spin structure with periodicity 62 nm, this cancels any macroscopic magnetic moment in the compound. One way to break this periodical structure is either by dimensional limitations, such as thin film, or by doping with rare earth elements. The latter is due to the strong magnetic moments of many rare earth elements, and recent works have shown promising results for $BiFeO_3$ doped with lanthanum [10, 15].

Le Bras *et al.* [10] performed magnetization and magnetocapacitance measurements on ceramic samples of $Bi_{1-x}La_xFeO_3$ for $0 \leq x \leq 0.25$ and found La doping to significantly reduce the transition magnetic field from the spatially modulated state and increase the magneto-capacitance. Figure (figur 2.14a) shows the magnetic field dependence of the normalized dielectric constant of samples with different La-dopant concentration, with a relative enhancement of 0.14% for $x = 0.15$ around 8 T. Figure (figur 2.14b) shows the dopant dependence normalized dielectric constant of the 8 T value. The reduced constant at $x \geq 0.17$ was attributed to the lattice symmetry gradually changing from rhombohedral ($R3c$) to orthorhombic (C222), the latter known to be a crystal structure without magnetoelectric effect [15].

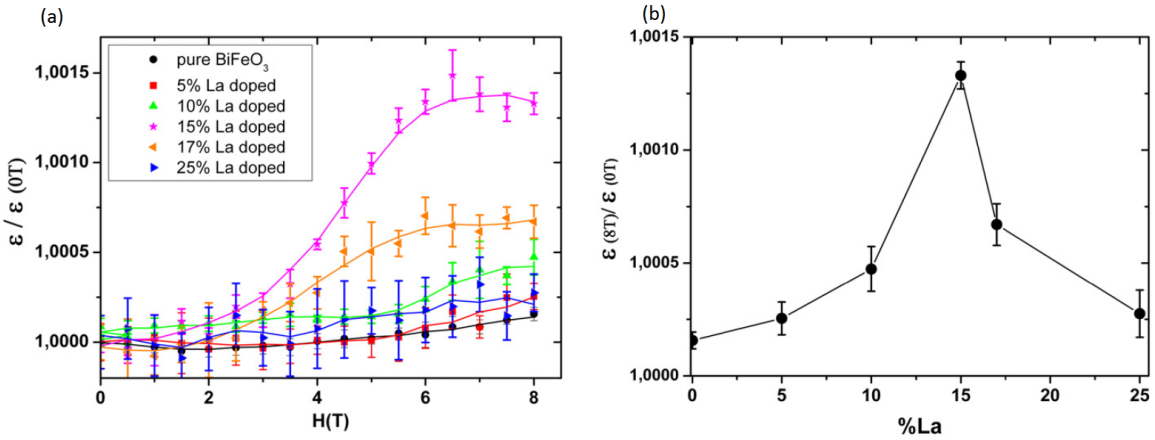

Figure 2.14: (a) Magnetic field dependence of the normalized dielectric constant in the $Bi_{1-x}La_xFeO_3$ series at 1000K. (b) Dependence on La content of the 8 T value of the normalized dielectric constant [10].

2.5 Finite size effects

Multiple reports on different compositions have addressed a finite crystallite size in which the ferroelectric state becomes unstable [6, 7, 8, 61]. The origin of size effects in fine particles are debated, but typical examples of models are: (1) the particle must be in a single domain state when it is smaller than the domain thickness and the depolarization field makes the ferroelectric state unstable; (2) the pressure in the small particles varies in inverse proportion to the particle diameter due to the surface tension [29]. Several phenomena occurs at the point where the particle or crystallite size reaches a critical value.

2.5.1 Lattice parameters

Size effects in ferroelectric materials have been investigated theoretically and experimentally for a long time [8]. As the crystallite size decreases, the axial ratio $\frac{c}{a}$ of tetragonality and the ferroelectricity decreases in $BaTiO_3$ nanocrystals, and the ferroelectric phase vanishes at a critical size of 48 nm [62]. At sizes below 100 nm, the tetragonality of $PbTiO_3$ shows a strong dependence on the crystallite size, transforming into a paraelectric cubic phase ($\frac{c}{a} = 1$) at a critical size of 7.0 nm.

Selbach *et al.* [5] observed a similar dependence for $BiFeO_3$ nanoparticles prepared by modified the Pechini method (see figure 2.15).

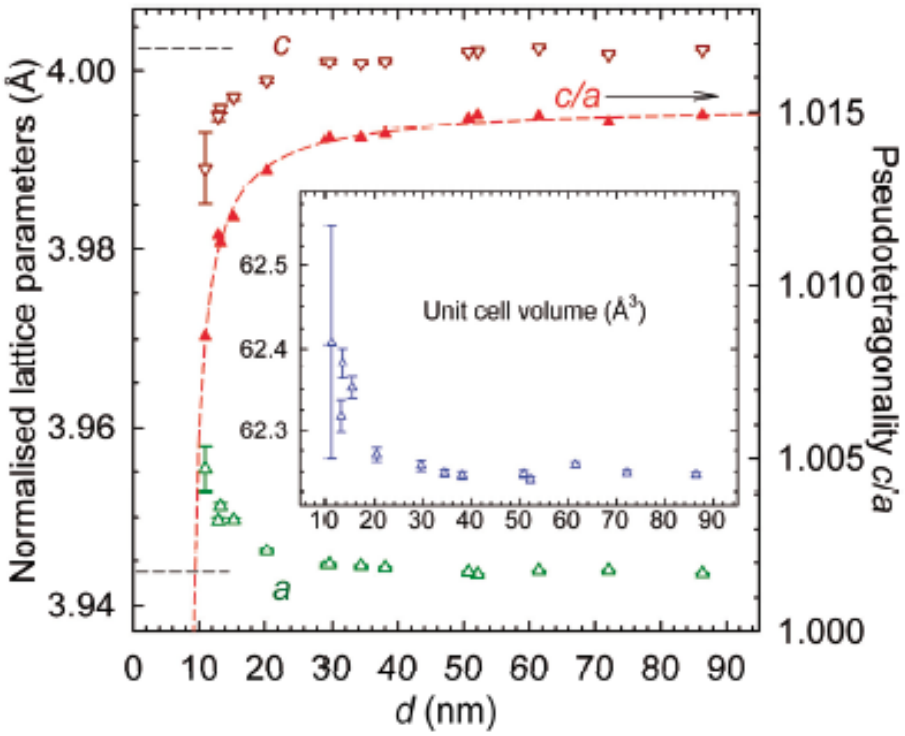

Figure 2.15: Normalized lattice parameters, a and c (open circles), and pseudotetragonality ($\frac{c}{a}$) (red triangles) in $BiFeO_3$ as a function of crystallite size. Inset: unit cell volume as a function of crystallite size. Arrows indicate bulk value [5].

The normalized pseudotetragonality went from bulk value towards unity as the

crystallite size decreased, with extrapolation indicating a critical size of 9 nm. The inset in figure 2.15 shows the unit cell volume as a function of crystallite size, and for sizes below ∼30nm the volume increases from the bulk value. This is due to the squared contribution from the a-parameter which increases in this region.

2.5.2 Cooperative cationic displacement, *s* - *t*

As explained in chapter 2.2.2, the displacement of the cations in $BiFeO_3$ can be described by the parameters s and t, these being polar displacement from the original positions of Bi^{3+} and Fe^{3+}, respectively. When doping the structure with a lanthanoid, this displacement is also seen to occur for the Ln ions on the Bi-sites [2]. The relative displacement of the cations, s - t, is equal to Δz_{hex} of Fe^{3+} with Bi^{3+} fixed at z = 0. The rhombohedral, ferroelectric perovskites $LiNbO_3$ and $LiTaO_3$, isomorphous with $BiFeO_3$, both show a linear relation between Δz_{hex} of Nb/Ta cation and the spontaneous polarization, P_S. In $BiFeO_3$, the main source of P_S is the displacement of Bi^{3+} caused by the stereochemically active $6s^2$ lone pair [45]. First-principle studies indicates that the displacement of Bi^{3+} is responsible for approximately 98.5% of the total spontaneous polarization [46], making the cooperative displacement a good basis for a crystallographic measure of polarization.

Selbach *et al.* [5] showed this relative displacement to be strongly dependent on the crystallite size of $BiFeO_3$ with a reduction of 25% from bulk down to 13 nm (figure 2.16). This was explained as being caused by increased depolarized field. Comparing the size-dependence of s - t with that of pseudotetragonality $\frac{c}{a}$ of the same structure, the size-effects of the former were more pronounced in larger crystallite sizes than in the latter. In crystallites of 30 nm, the s - t parameter deviated from bulk while $\frac{c}{a}$ did not.

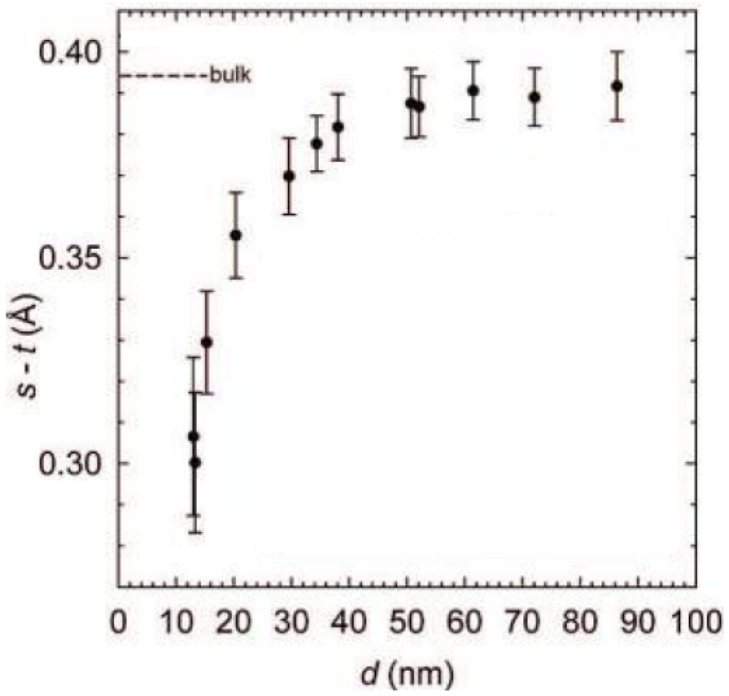

Figure 2.16: Cooperative displacement of Bi^{3+}/La^{3+} and Fe^{3+} expressed as s - t. Dashed line denotes value for bulk powder [5].

The data for cooperative cationic displacement in Ln-doped $BiFeO_3$ is very scarce, but some results show that the displacement is less effected by which cation occupies the Bi-site. Selbach [2] showed that the cationic displacement of $Bi_{0.9}La_{0.1}FeO_3$ was relatively equal that of undoped $BiFeO_3$, resulting in a relatively low contribution from the absence of the $6s^2$ lone pair inherent to Bi^{3+}.

2.5.3 Ferroic ordering

Several authors have reported change in the ferroic ordering due to size effects in different structures, observed through measurement of both Néel temperature as well as the Curie temperature at reduced dimensions [5, 6, 7, 8].

Sun *et al.* [7] studied the behavior of nickel nanowires, and observed a reduction in the Curie temperature of the wire from 360°C to 310°C with a diameter reduction from bulk to 30 nm. No final explanation were proposed except the note that the strain in the wires of reduced size could be one of the factors. Tanakaab *et al.* [6] observed a change in the Curie temperature of barium titanate particles from 400K to ∼190K as the particles were reduced from bulk values to 22 nm. They also noted that this was at the critical size for the structure, as they observed an orthorhombic-cubic transition occurring at smaller sizes.

Zheng *et al.* [61] studied the finite size effect on Néel temperature in antiferromagnetic nanoparticles and found the phase transition of ball-milled single CuO crystals to be reduced from 229K to ∼30K when reducing the size to ∼5 nm. This was lowered further to ∼13K as they observed this transition in nanorods of 2-3 nm in diameter. Doing measurements on T_N as a function of crystallite size, Selbach *et al.* [5] observed the antiferromagnetic to paramagnetic transition of the nanocrystallites at sizes below

$\sim$50nm. Figure 2.17a shows the temperature decreasing rapidly as the size goes towards the estimated crucial size of 9 nm. The inset in the same figure gives the heat flow as a function of temperature in samples calcined at different temperatures, thus of different sizes. Combining the results from the T_N measurements with those of the s - t, the relation between the phase transition and the cooperative displacement is observed. As seen in figure 2.17b, this yields a linear relation, indicating a strong coupling between the two phenomena. It was proposed that the antiferromagnetic ordering may be influenced by the polarization and possibly stabilized, in good agreement with related findings of dielectric and phonon anomalies at T_N [63].

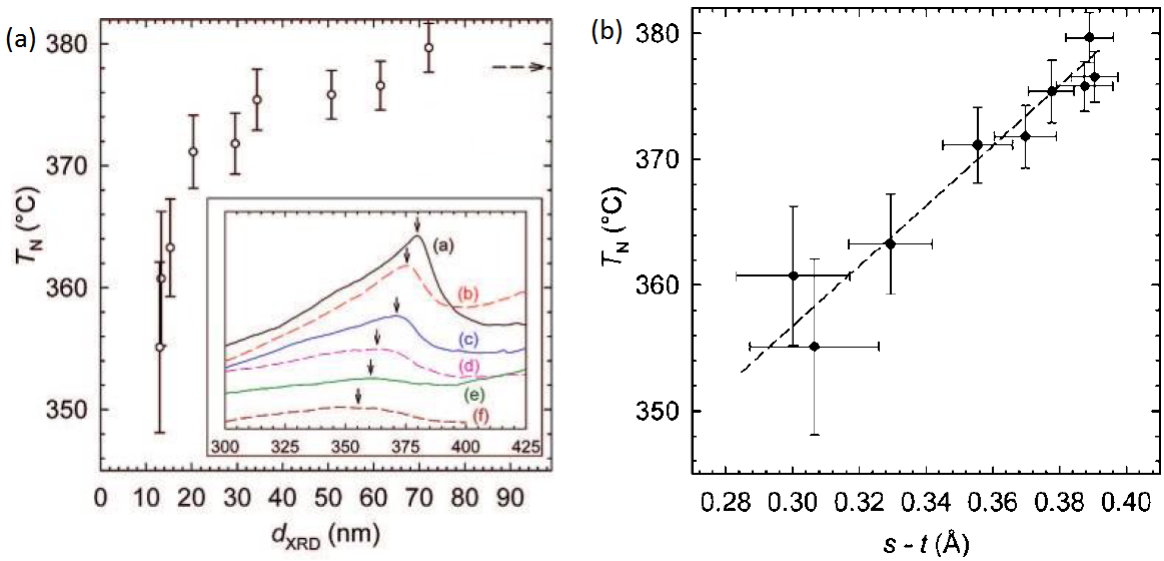

Figure 2.17: (a) Néel temperatures of nanocrystalline $BiFeO_3$ as a function of crystallite size. Inset: DSC traces for crystallite sizes of 13.0 nm to bulk, arrows denote peak position and T_N. (b) Comparing s - t and T_N for the same crystallite sizes gives a linear relationship; dashed line is a guide for the eye [5].

2.5.4 Doping $BiFeO_3$ with lanthanum

There are many reason for doping $BiFeO_3$ with lanthanum. Le Bras *et al.* [10] points out the destruction of the space-modulated spin cycloid by making it energetically unfavorable as important, along with the increase in the magneto-capacitance (seen in figure 2.14). Selbach [2] points out the substitution with lanthanum as detrimental to ferroelectricity as the unit cell distortion and ferroelectric Curie temperature decreases with increasing La content.

But little work has been done on the size-effects of lanthanum doped $BiFeO_3$. Hatling [24] performed measurements on $Bi_{0.9}La_{0.1}FeO_3$ with crystallites calcined at temperatures between 400°C and 850°C, but were unable to observe crystallites of sizes below $\sim$30 nm. Compared to bulk, only small variations of the normalized cell parameters , a and c, the unit cell volume and the Néel temperature were observed at the smallest sizes. The minute changes in the mentioned observations were explained by the absence of $6s^2$ lone-pairs in La^{3+}-ions, enabling the structure to sustain small crystallite sizes without an abrupt change in lattice parameters.

3 Experimental

3.1 Synthesis

$Bi_{0.9}La_{0.1}FeO_3$ nanocrystallites were prepared through wet chemical syntheses with aqueous nitrate solutions as metal precursors. This was done by dissolving the three metal powders, $Bi(NO_3)_3{\cdot}5\,H_2O$ (Fluka, >98%), $Fe(NO_3)_3{\cdot}9\,H_2O$ (Sigma Aldrich, >98%) and $La(NO_3)_3{\cdot}5\,H_2O$ (Merck, >99%) in distilled water in separate containers, reducing the pH to around 1 with the addition of HNO_3 (Merck, 65%) to prevent precipitation and thus loss of metal cations. To determine the exact cation concentration in the different precursor solutions, a standardization was done. At first, 12 porcelain crucibles and four samples of each cation solution were weighed separately and heat treated at 800°C (600°C for bismuth nitrate) for 24 h. The low annealing temperature for the bismuth solution was to minimize the risk of loss of volatile bismuth oxide, and to prevent boiling, and thus loss of cations. A heating rate of 50°C/h was chosen, and the total weight of the separate porcelain crucibles were weighed after being cooled to room temperature.

The synthesis of $Bi_{0.9}La_{0.1}FeO_3$ was done through modified Pechini method by replacing equal cationic molar amount of $Bi(NO_3)_3{\cdot}5\,H_2O$ with $La(NO_3)_3{\cdot}5\,H_2O$. As complexing agent the carboxylic acid DL-tartaric acid (Acros Organics, 99.5%) was prepared by dissolving it in distilled water with a molar concentration higher than the metal precursors to ensure complete complexation. To ensure that the carboxylic acid was completely dissolved, the distilled water was heated to 50°C before introducing the acid and allowed to stir on a hot plate for several minutes. Ethylene glycol (Acros Organics, >99.9%) was prepared for use as a polymerizing agent. Both DL-tartaric acid and ethylene glycol were added with a ratio of 2:1 to the cations.

Having prepared all solutions the dissolved metal precursors were separately weighed, poured and mixed together in a crystallization jar; the molar ratio La:Bi:Fe being 1:9:10. The complexing agent was then added to the precursor mix, and after some minutes of complexation the ethylene glycol was poured slowly into the solution. The crystallization jar containing the mix was put on a hot plate holding 130°C, and to ensure homogeneous solution a magnetic stirrer was used while the solution was still in the liquid state. After thermal treatment for several hours the dried residue had a firm and porous texture and a brown color. It was then milled into a fine powder in an Agate mortar and calcinated at different temperatures to study the thermal effect on the structure and crystallite size. This was done in a calcining furnace (Naberferm Furnace, P320). The heating rate was divided into four intervals; from room temperature to 400°C it was 100°C/h, then it was held at this temperature for 30 minutes, then a rate of 200°C/h up to the final temperature before it was held at this temperature for 3 hours. The final temperature varied from 400°C to 850°C and is denoted T_{cal}.

3.2 Characterization

3.2.1 X-ray diffraction

An X-ray diffractometer (XRD, θ-2θ Bruker AXS D8 ADVANCE) with a LynxEye positioning sensitive detector (PSD) was used at room temperature using a 0.2° fixed

divergence slit. Data was collected by a scan from 20° to 90° 2θ with a step size of 0.02°, 3 seconds per step (total data collection time 3 h 5 min per sample).

3.2.2 Rietveld refinements

All Rietveld [64] refinements were carried out using TOPAS R (Bruker AXS) version 4.2 software. An input-file of 2θ hkl-values of phase pure $BiFeO_3$ ($R3c$) was loaded for each XRD peak profile, and background intensity was refined using a Chebychev polynomial of the minimum order to account for the curvature. Sample displacement were also refined, while zero errors were fixed. Each peak profile were computationally measured relative to the input-file, and the data profiles were calculated until the fit converged to the best value. The refinement gave both the crystallite size as well as the lattice parameters, c and a, for each peak profile. For calculating the crystallite size, full width at half maximum (FWHM) based LVol calculation were used, this by assuming intermediate crystallite size broadening modeled by a Voight function. This method was kept for all measurements. For direct comparison with the aristotype structure the normalized lattice parameters were used to calculate the pseudotetragonality. For measuring atomic positions, the positions of the heaviest atom in the unit cell were refined to convergence before subsequently adding lighter atoms to the refinement.

3.2.3 Differential scanning calorimetry

Differential scanning calorimetry (DSC) was performed using a Perkin Elmer DSC 7, PE Thermal Analysis Controller TAC/DX with Pyris version 3.81 software. The mass of the samples varied between 20 - 50 mg and were encapsulated in small aluminum sample pans. Each selected sample was sequentially heated and cooled in air from room temperature to 425°C three times, this to extract a more representative data set of the heat flow. The heat rate was 40°C/min, and the Néel temperature was determined by examine the maximum values of the colorimetric peaks as a function of temperature.

3.2.4 Differential thermal analysis

Differential thermal analysis (DTA) was performed using a Netzsch STA 449 C Jupiter in air in the temperature region 30 - 850°C. Both cycles had a heating/cooling rate of 40°C/min. The sample varied between 50 - 150 mg and alumina crucibles were used to hold the samples during analysis. First order phase transitions were determined at the onset of the thermal events.

4 Results

4.1 Synthesis and X-ray diffraction

In this work, several different syntheses has been made, although of different quality. As some of them have shown to contain much of secondary phases, the focus have been on the two syntheses which gave observable data. The rest of the work will therefore only contain measurements based on data from these two syntheses.

The two syntheses given here were both synthesized by the modified Pechini method used in literature [2, 24]. After each synthesis the green powder were calcined up to 400°C to ensure that all organic residue was removed before XRD was used to determine crystallographic structure of the powder. Figure 4.1 shows XRD patterns of powder from synthesis 1 (a) and synthesis 2 (b) at different temperatures.

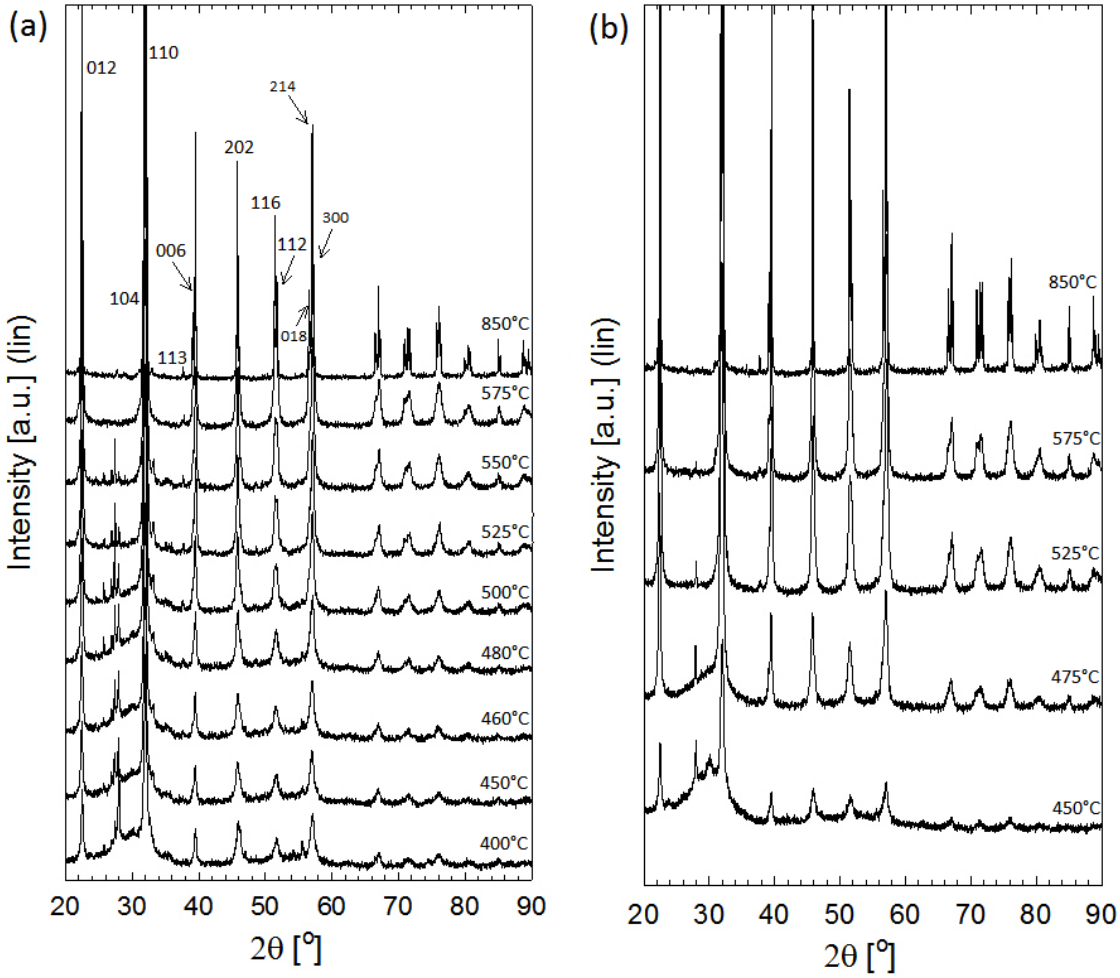

Figure 4.1: XRD patterns of powder from (a) synthesis 1 and (b) synthesis 2 calcined at different temperatures. Miller indices giving the {hkl} phases from literature are labeled in (a) [2]. Reflections around 28 2θ is from secondary phases. The calcining temperature is given above each pattern.

In figure (a) the Miller indices giving the {hkl} planes from literature at bulk values are given [5]. Synthesis 2 was calcined at higher temperatures due to the observed

secondary phases at temperatures of 450°C in synthesis 1.

4.2 Structure

4.2.1 Crystallite size and lattice parameters

All XRD patterns from synthesis 1 and 2 were refined using the TOPAS software. Although the software automatically detected phases inherent to the $BiFeO_3$ structure, manually labeling of the secondary phases was needed for some patterns. In this way, only the contribution to the crystallite size from the former structure was measured.

Figure 4.2a shows how the size of the crystallites changes as the calcining temperature is increased, with crystallites from both the measured syntheses growing as expected. In figure 4.2b the size of the crystallites are plotted against their normalized lattice parameters, a and c, separated by synthesis.

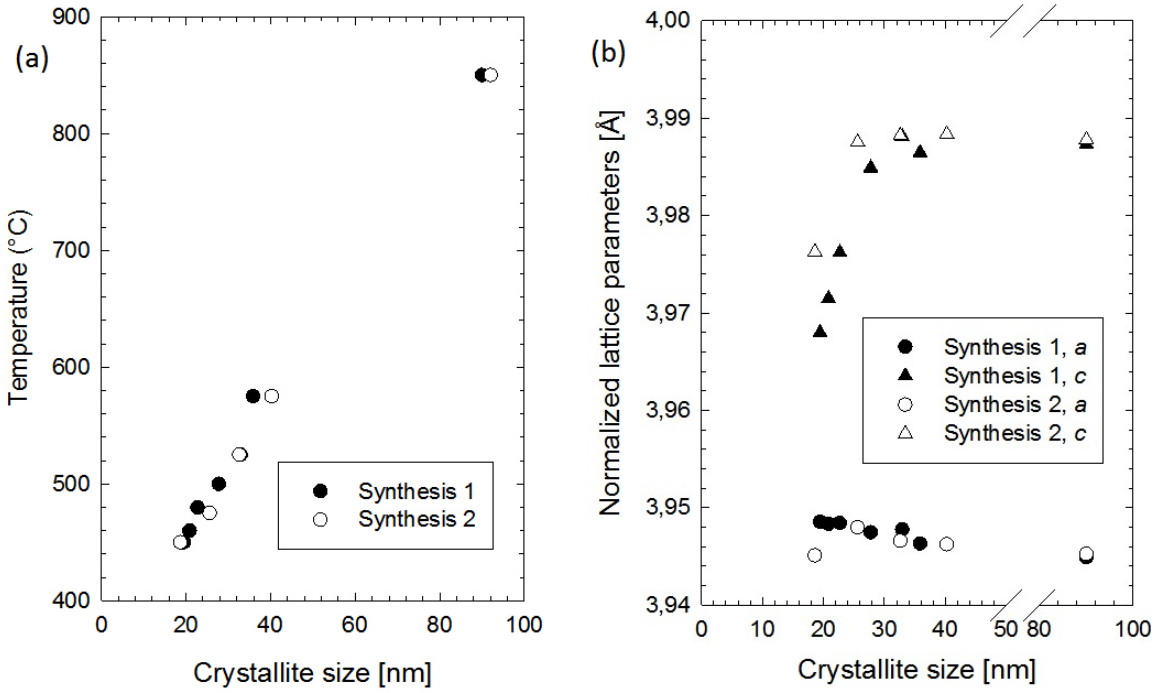

Figure 4.2: Comparing the crystallite size for synthesis 1 and 2 to (a) the calcined temperature and (b) the normalized lattice parameters, a and c.

4.2.2 Pseudotetragonality and unit cell volume

From the data in figure 4.2b, the pseudotetragonality $\frac{c}{a}$ can be calculated as a function of crystallite size of the different syntheses. The unit cell volume is calculated from the equation

$$V_{cell} = c * a^2 \tag{4.1}$$

where V_{cell} is the volume of the normalized unit cell with c and a as lattice parameters. This data is given in figure 4.3.

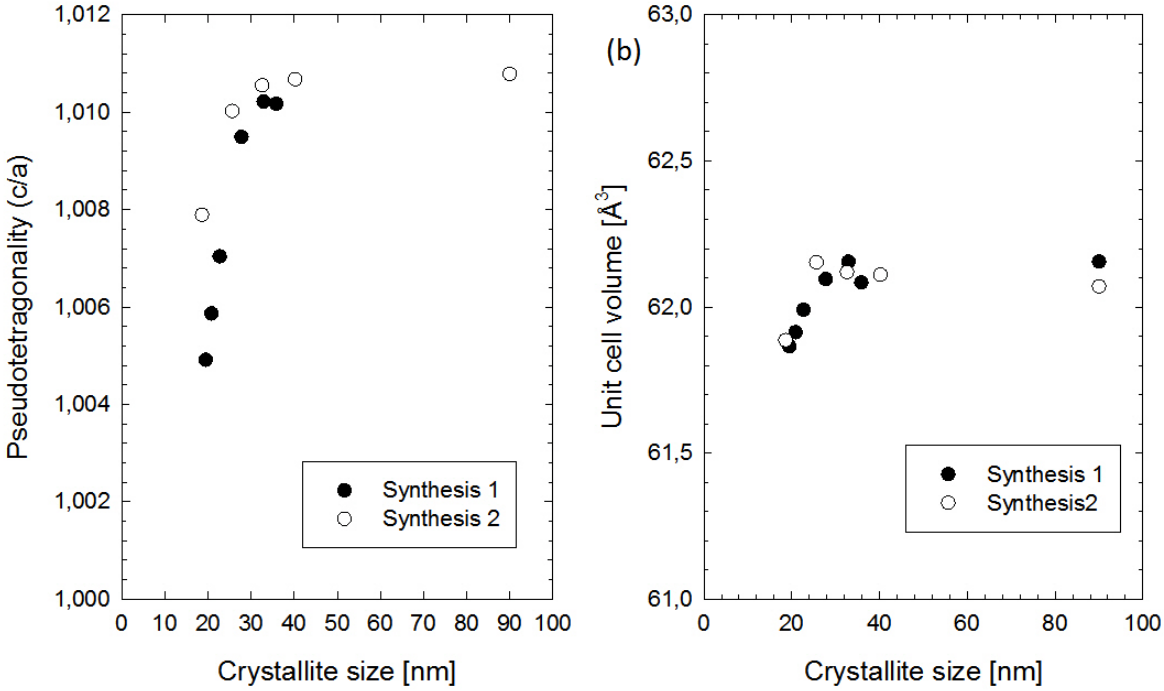

Figure 4.3: Comparing the crystallite size for synthesis 1 and 2 to (a) the pseudotetragonality $\frac{c}{a}$ and (b) unit cell volume.

4.2.3 Cooperative cationic displacement, *s* - *t*

Rietveld refinement of the selected samples gave the cooperative cationic displacement between Bi^{3+}/La^{3+} and Fe^{3+}, *s* - *t*, as a function of crystallite size. This is plotted in figure 4.4.

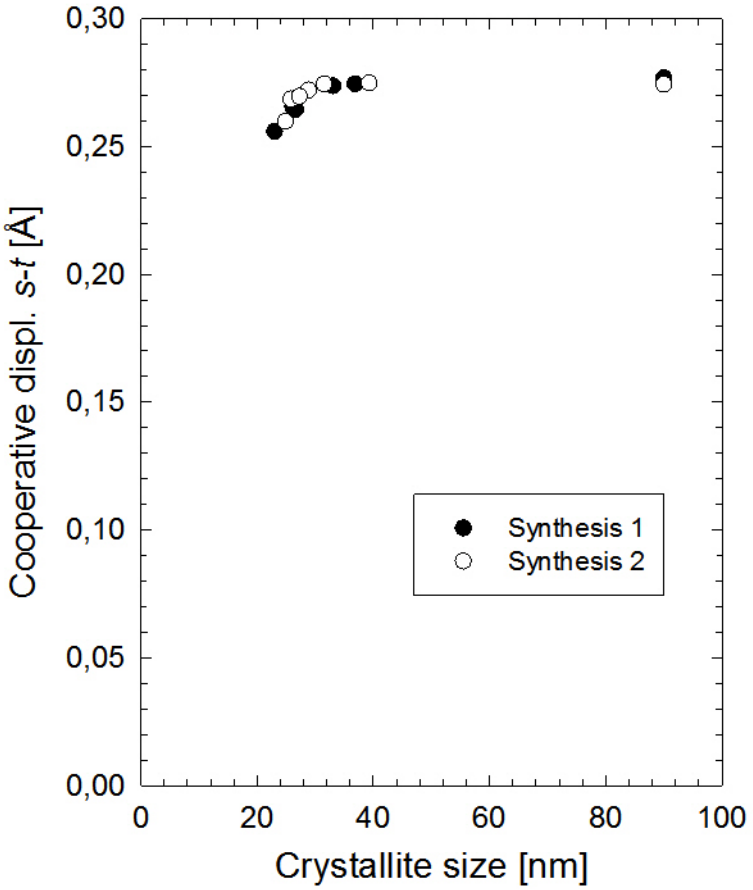

Figure 4.4: The cooperative displacement of Bi^{3+}/La^{3+} and Fe^{3+}, s - t, as a function of the crystallite size for both synthesis.

4.3 Néel temperature

The Néel temperature was determined using differential scanning calorimetry on selected samples from the two syntheses. Figure 4.5 shows the heat flow of each synthesis as a function of temperature during (a) heating and (b) cooling. The region was limited to T = [350, 420] as this was the range were cusps were observed for all samples indicating a Néel temperature. Arrows depict the estimated T_N, and these values are shown in figure 4.5(c) both for heating and cooling, with given errors due to the width of the peaks.

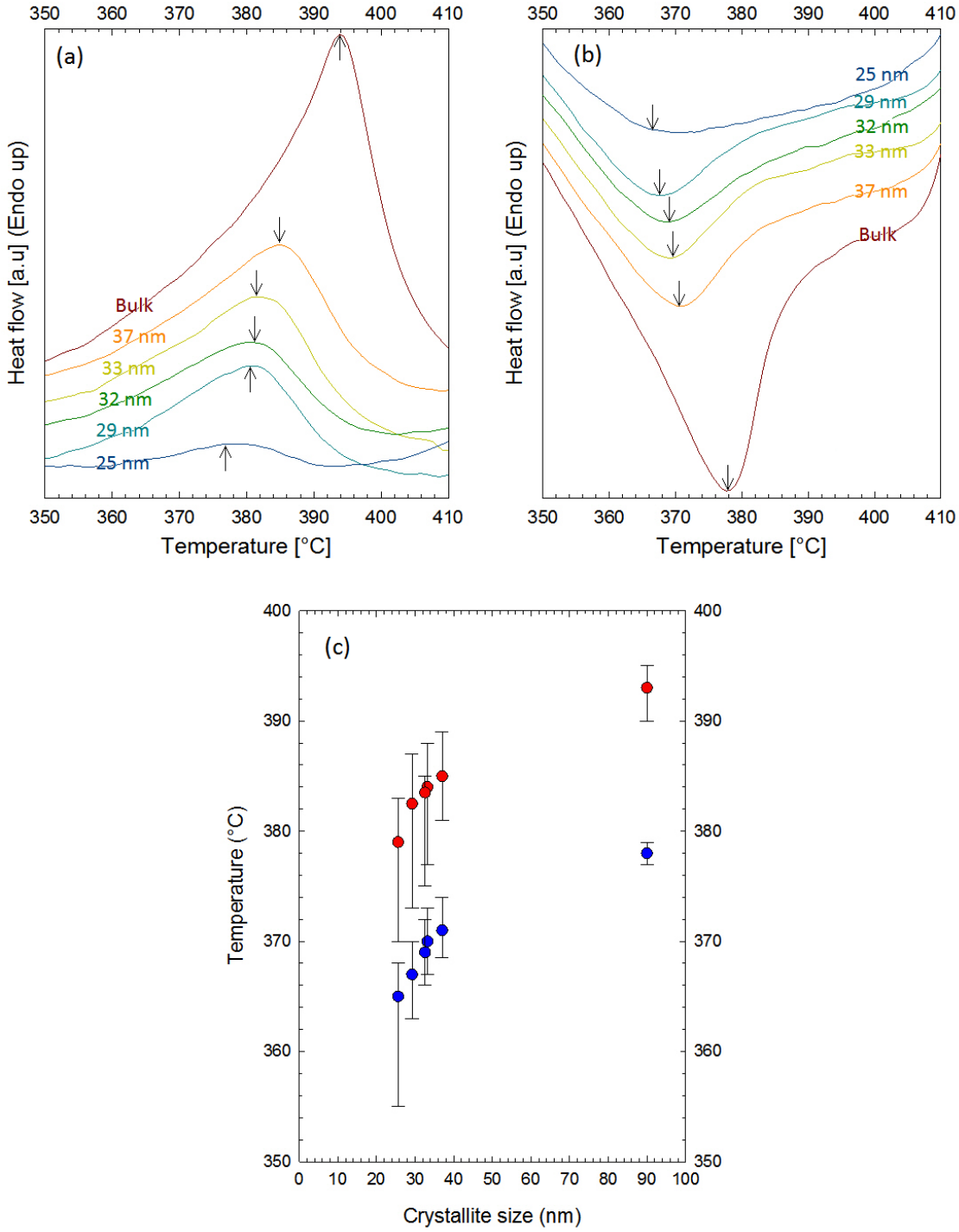

Figure 4.5: DSC traces of bulk and nanocrystalline $Bi_{0.9}La_{0.1}FeO_3$ measured in air with a heating rate of 40°/min for (a) heating and (b) cooling. Arrows depict the estimated T_N. (c) T_N as a function of crystallite size: (red) heating and (blue) cooling.

4.4 Curie temperature

The Curie temperature was determined using differential thermal analysis on selected samples from both syntheses. Figure 4.6a shows the results from the analysis in the

range of the phase transition, while 4.6b includes more of the data at lower temperatures. A total of three samples were analyzed twice at a heat rate of 40°C/min. As the final temperature was above the calcined temperature of each sample, the second run for each sample was assumed to show properties of bulk-like structure due to crystallite growth at these temperatures. All second runs are represented by the same plot (red) in both figures due to similar behavior at the exact same temperature. This also applied to the cooling plot which is represented by the top-most plot in both figures (pink). This temperature was observed for all samples at both runs.

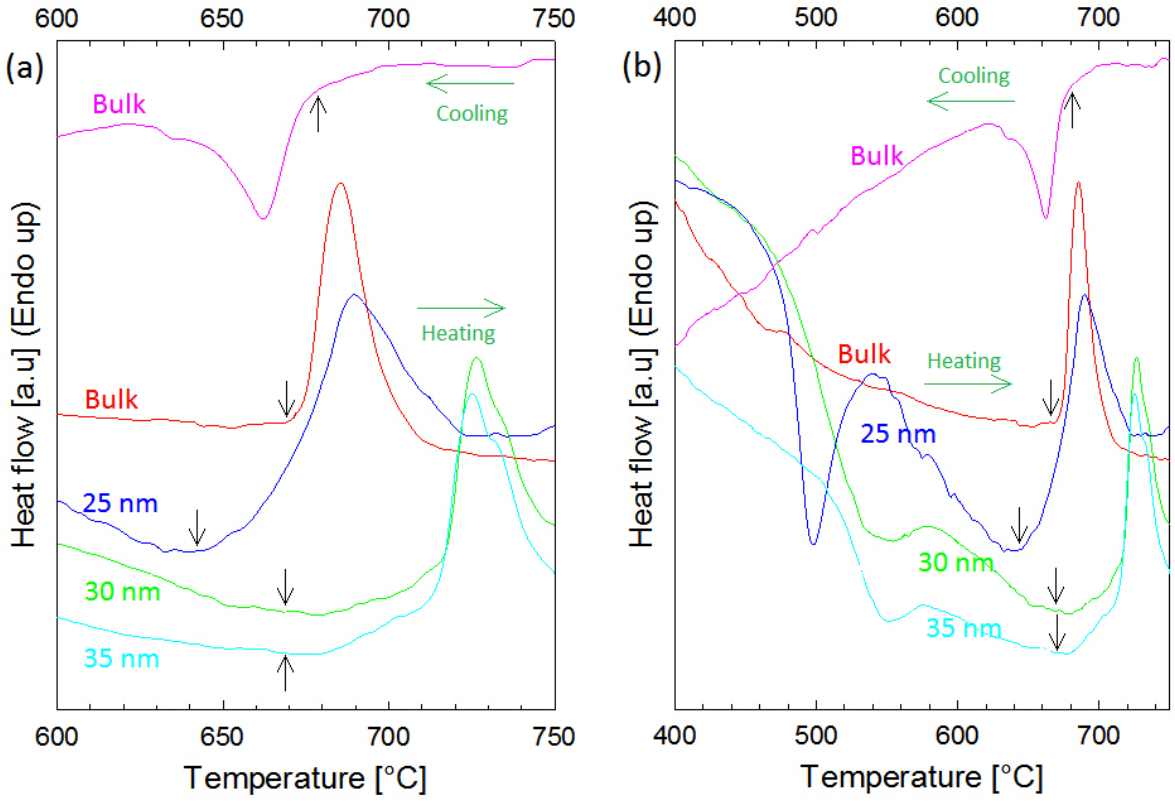

Figure 4.6: DTA traces of bulk and nanocrystalline $Bi_{0.9}La_{0.1}FeO_3$ powders measured in air with a heating rate of 40°/min. Both red and pink traces are bulk values equal for all samples by heating and cooling, respectively. Arrows depict the estimated T_C. (a) is zoomed in, while (b) includes data at lower temperatures.

5 Discussion

5.1 Synthesis and X-ray diffraction

5.1.1 Synthesis

The parameters used for all syntheses were based on earlier work by Selbach [2] and Hatling [24]. As the former work showed that several carboxylic acids were useful as complexing agent for $BiFeO_3$, the latter work produced phase pure $Bi_{0.9}La_{0.1}FeO_3$ using primarily DL-tartaric acid. Also the concentrations of metal precursors, ethylene glycol and the given carboxylic acid were unchanged from Hatling [24], as well as the heat treatment process during gelation of the solution. Earlier work have observed a broad exothermic effect with a major weight loss around 380°C using thermogravimetry (TG) and has been assigned to the decomposition of the trapped nitrates and carbonaceous matters [24, 35]. As a result of this, the lowest temperature used for calcining was 400°C. Figure 5.1a compares the XRD pattern of synthesis 1 calcined at 400°C with results on $Bi_{0.9}La_{0.1}FeO_3$ by Hatling. The pattern from synthesis 1 shows a growth of crystallites at a lower temperature compared to [24]. Already at 400°C, peaks representing the different phases are visible, while crystallites are first seen to grow at temperatures above 450°C in the reference. Secondly, 2θ-angles in which the larger peaks are occurring does not fit with the refraction angles for $Bi_{0.9}La_{0.1}FeO_3$ (JCPDS no. 86-1518), but rather the reflections for the bismuth-rich phase $Bi_{25}FeO_{39}$ (sillenite). These peaks are not seen in the reference pattern.

Selbach [2] observed similar peaks occurring in $BiFeO_3$ calcined at 600°C and explained them as being the result of ignition during calcination caused by a too rapid heating. Both Hatling [24] and this work uses a slower heating rate than Selbach, so the observations of bismuth-rich phases being present in the powder was not assumed to be inflicted due to ignition.

For synthesis 2, a new Fe-solution was prepared in the same way as described in chapter 3.1, and a new standardization of all cationic solutions was performed to verify the exact concentration. The concentration was the same for the Bi- and La-solution, and the parameters for the synthesis was not changed compared to synthesis 1. As can be seen from figure 5.1b and c, synthesis 2 show a similar pattern as synthesis 1 for all temperatures. Although traces of secondary phases are present in patterns from both syntheses, they are of high enough quality to do qualitatively observations on cell-parameters, unit cell volume, cooperative cation displacement (s-t) as well as determine Curie and Néel temperature as a function of crystallite size.

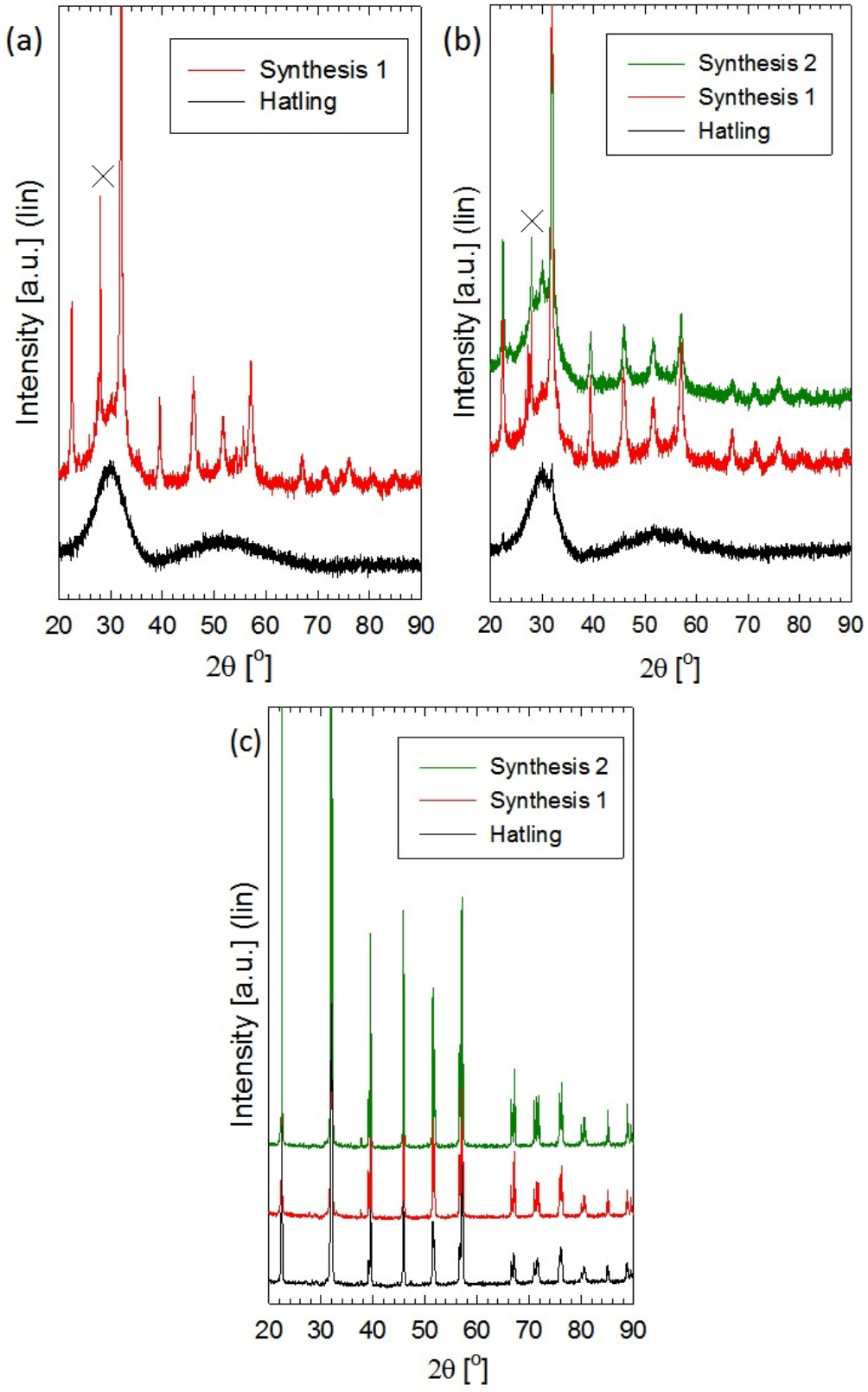

Figure 5.1: A comparison between synthesis 1 (red), synthesis 2 (green) and Hatling [24] (black) of $Bi_{0.9}La_{0.1}FeO_3$ calcined at (a) 400°C, (b) 500°C and (c) 850°C. "X" marks the secondary phases in (a) and (b).

5.1.2 Peak position

As explained in chapter2.1.1, increased calcination temperature will increase crystallite sizes. In addition, having $Bi_{0.9}La_{0.1}FeO_3$ crystallites of homogeneous sizes allows for the investigation of size-dependent properties reported on $BiFeO_3$ [2, 64]. For the XRD patterns of both syntheses, labeling of the secondary phases was important in order to calculate the crystallite size of the perovskite phase.

Comparing these results with Hatling [24], figure 4.1 shows peaks occurring at similar positions inherent to the perovskite structure. Both patterns show a broad amorphous peak in the range 25 - 35 2θ, although some secondary phases are visible in syntheses 1 and 2. As the calcining temperature increases, the peaks become narrower and the intensity increases at the perovskite Bragg diffraction lines indicating a increasingly crystalline structure and crystallite growth. Reflection splitting from the rhombohedral distortion of the unit cell appear in the XRD pattern of crystallites calcined at high temperatures due to the combined effect of decreased unit cell symmetry and peak narrowing (see figure 4.1). The top most pattern for all syntheses is powder calcined at 850°C, and the location of the peaks along with the high intensity indicates large crystallites of bulk size in accordance with literature (JCPDS no. 86-1518) [2, 24, 49]. This is in good compliance with earlier results on $BiFeO_3$ and indicates a similar behavior of the lanthanum-doped structure.

5.2 Structure

As it has been shown that syntheses 1 and 2 behave in a similar way in the same size-region, the rest of the work will use data from both and label them as "this work".

5.2.1 Crystallite size

The dependence of temperature on crystallite size is shown in figure 4.2 and confirms the increase in size as a function of T_{cal}. Selbach *et al.* [5] and Ghosh *et al.* [36] showed a similar trend of $BiFeO_3$ synthesized by modified Pechini method (figure 5.2) with a wider range of crystallite sizes, Haneberg [50] observed the growth of crystallites as a function of temperature in $Bi_{0.9}Sm_{0.1}FeO_3$, while Hatling [24] showed a similar trend with $Bi_{0.9}La_{0.1}FeO_3$. The use of Scherrer equation [65] instead of TOPAS software may have caused the measured sizes to have the wide range seen in the two former works. Park *et al.* [64] also used the Scherrer equation in his work on single-crystalline $BiFeO_3$.

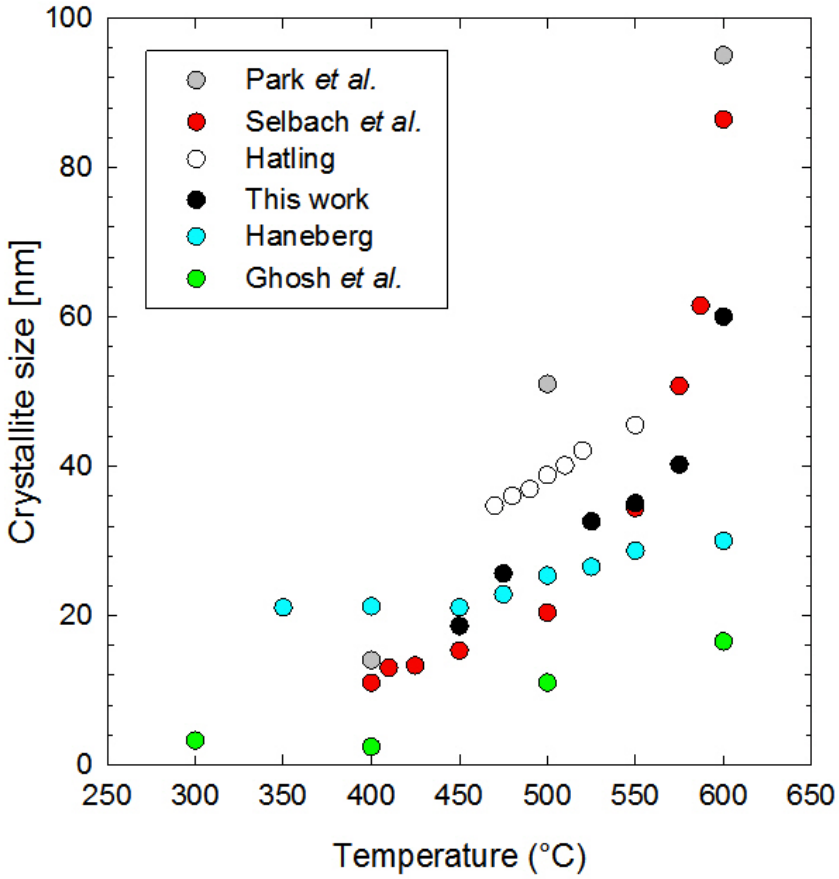

Figure 5.2: Crystallite size as a function of T_{cal} for: (gray) Park *et al.* [64]; (red) Selbach *et al.* [5]; (white) Hatling [24]; (black) this work; (cyan) Haneberg [50]; (green) Ghosh *et al.* [36]. All authors show the crystallite size increase with increased calcining temperature.)

5.2.2 Lattice parameters, *a* and *c*

There has been little work done on the structure of nanocrystalline $BiFeO_3$, as well as $BiFeO_3$ doped with rare earth metals, as a function of crystallite size. Most of the work is done at temperatures in which the powder is showing bulk-like properties, thus ignoring the change in lattice parameters with reduced crystallite size. Figure 5.3 compares data from this work (figure 4.2b) alongside results from Hatling [24], all done on $Bi_{0.9}La_{0.1}FeO_3$. The values for normalized lattice parameters coincides for both *a* and c. The figure also compares this data with that of Selbach *et al.* [5] and Haneberg [50], the former observed a transformation in undoped $BiFeO_3$ from the rhombohedrally distorted perovskite structure towards a ideal, cubic perovskite structure at decreasing crystallite sizes, while the latter the same on samarium doped $BiFeO_3$.

From this figure several things are clear. Firstly, the bulk values of the *c*-parameter for all syntheses of Ln-doped $BiFeO_3$ are lower than that of undoped $BiFeO_3$, whereas the *a*-parameter is more equal. Secondly, the trend of both normalized lattice parameters behaves in the same constant way for all structures down to a crystallite size of ~30 nm. Above this size, no significant change in the values are measured. Below this

value, the undoped and Ln-doped $BiFeO_3$ crystallites follow the same size-dependency in the c-parameter of the doped structure, although at a larger crystallite size. This may be attributed to the measurement method, as the Scherrer equation was used in the former. The reduction in a-parameter for Sm-doped $BiFeO_3$ at crystallites smaller than 30nm may be due to a ionic radius of the cation, and is discussed elsewhere [50].

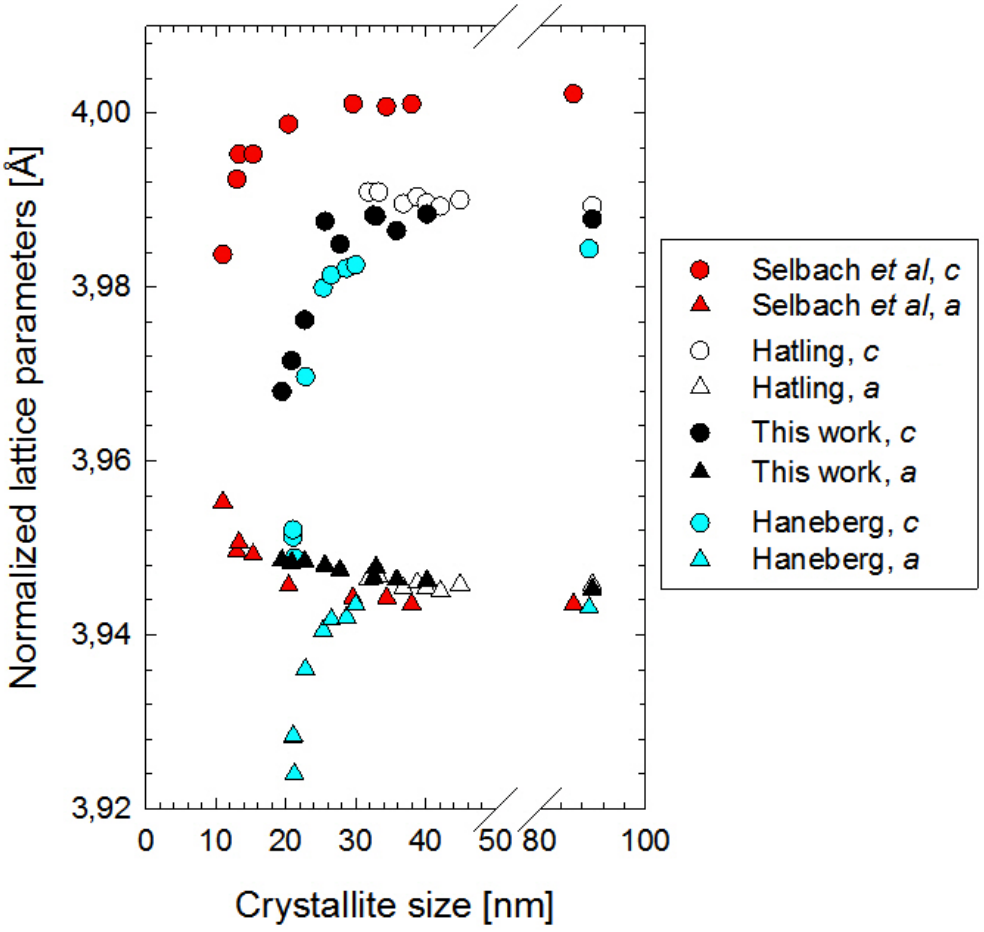

Figure 5.3: The normalized lattice parameters c (circles) and a (triangles) as a function of crystallite sizes for: (red) Selbach *et al.* [5]; (white) Hatling [24]; (black) this work; (cyan) Haneberg [50]. The former parameter follows the same trend for all compositions, while the latter is decreasing for samarium substituted $BiFeO_3$ as crystallite sizes decrease.

Selbach [2] observed this difference in the c-parameter between La-doped and undoped $BiFeO_3$ increasing with increased La-doping at bulk size crystallites. As the lattice parameter c is along the polar direction of the unit cell, it is more sensitive to La-doping than the a-parameter normal to the direction.

5.2.2.1 Pseudotetragonality The pseudotetragonality $\frac{c}{a}$ is a measure of the instability of the ferroelectric state. A value approaching unity corresponds to an ideal, cubic perovskite where the normalized lattice parameters are equal. Figure 4.3 shows the different syntheses with a clear size-dependence for sizes below 30 nm. Compar-

ing these results with data from Hatling [24], it is clear that this work show a similar behavior at crystallite sizes above 30 nm.

Figure 5.4 compares these results with those of Selbach *et al.* [5] and Haneberg [50] done on undoped and Sm-doped $BiFeO_3$, respectively, and it coincides with the results shown in figure 5.3 of the normalized lattice parameters, a and c. Even though this is expected based on the similar parameters, the values for Ln-doped $BiFeO_3$ are significantly lower and closer to unity than those of the undoped $BiFeO_3$. This is due to the lower bulk values for the c-parameter seen in figure 5.3 for all Ln-doped $BiFeO_3$ as well as the constant behavior of the a-parameter. From these observations, Ln-doped $BiFeO_3$ seems to respond to change in crystallite as undoped $BiFeO_3$; moving towards ideal, cubic perovskite structure.

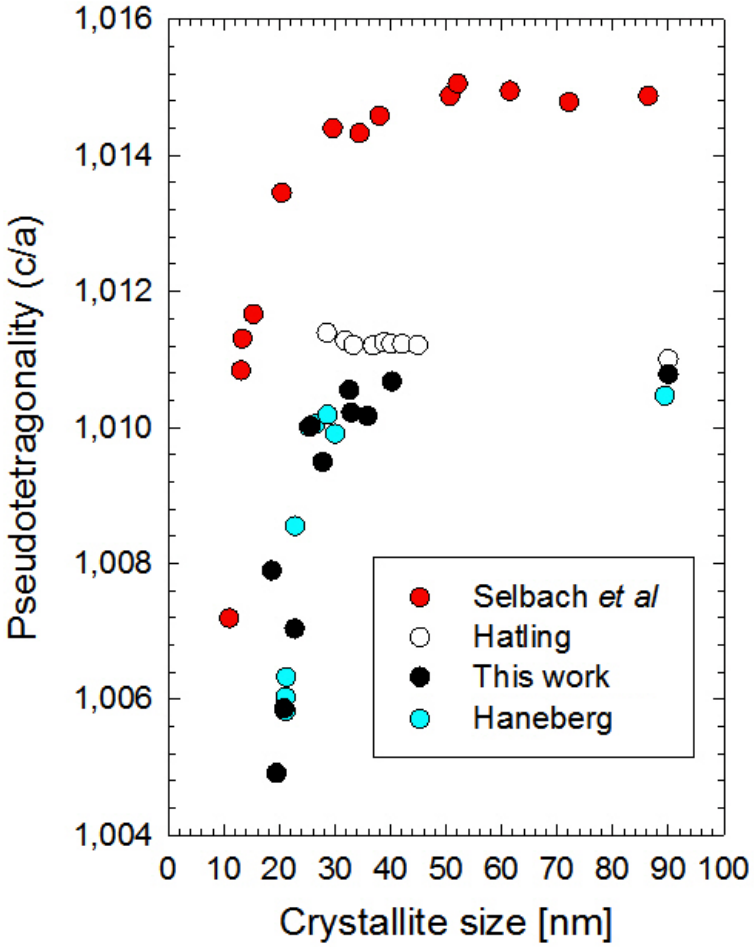

Figure 5.4: Pseudotetragonality ($\frac{c}{a}$) as a function of crystallite size for: (red) Selbach *et al.* [5]; (white) Hatling [24]; (black) this work; (cyan) Haneberg [50]. A strong dependence between ($\frac{c}{a}$) and size is observed for all compositions below ~30 nm.

5.2.2.2 Unit cell volume The data in figure 4.3 is calculated using equation 4.1 based on the values of the normalized lattice parameters, a and c. The trend of increased unit cell volume for decreasing crystallite sizes are visible for this work, and the small deviation from the bulk value for crystallites smaller than 35 nm is typical for partly

covalent oxides [66]. The uncertainties in measuring the normalized lattice parameters at small crystallite sizes may cause the sudden drop seen for sizes below 25nm.

In figure 5.5, a comparison is made with the results provided by Hatling [24], Selbach [2, 5] and Haneberg [50]. For all crystallites doped with lanthanum, the unit cell volume is always smaller than undoped $BiFeO_3$ due to the reduced c-parameter caused by to the polar direction of the unit cell and the relatively constant a-parameter seen in figure 5.3. This was also observed by Selbach in $Bi_{0.9}La_{0.1}FeO_3$, and shown in the figure (pink). In the work of Haneberg, a decrease in volume is visible through the whole range. It is difficult to explain why the unit cell volume is reduced as no other factors other than Ln-doping is present, and this would contribute to a larger volume as theorized.

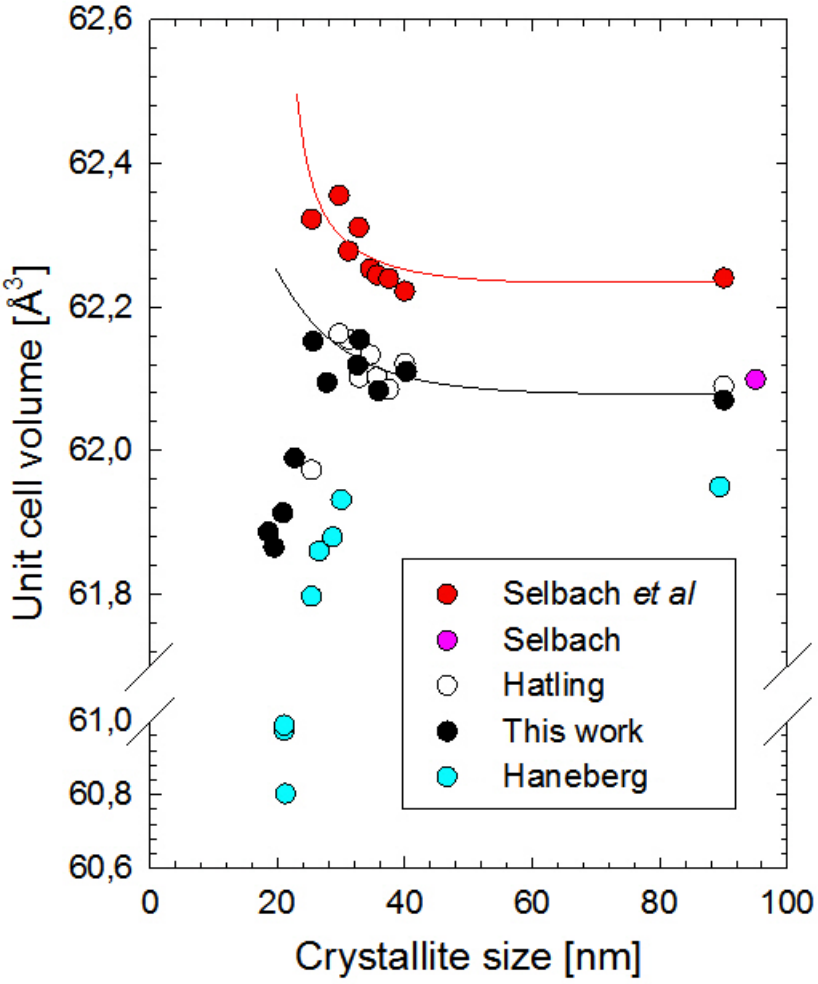

Figure 5.5: The unit cell volume as a function of crystallite size for: (red) Selbach *et al.* [5]; (pink) Selbach [2]; (white) Hatling [24]; (black) this work; (cyan) Haneberg [50]. An increase in the cell volume is observed for the four former compositions above ∼25 nm, while decreasing in samarium substituted $BiFeO_3$. This decrease might be due to measurement errors. Red and black lines are guides to the eye.

5.2.3 Cooperative cationic displacement, *s* - *t*

The displacement of the bismuth and iron cations, s and t respectively, are depicted in figure 2.4c and is assumed to be a good crystallographic measure of polarization [5]. By doping $BiFeO_3$ with lanthanum, a reduction in the lattice parameter c has been observed due to the missing $6s^2$ lone pair in La^{3+}, but this has earlier shown not to affect the bulk value of the cooperative displacement [2].

Figure 4.4 shows the displacement as a function of crystallite size, and a decrease is noticeable below ~30 nm showing a size dependence. A comparison of these results with those of Selbach *et al.* [5] and Haneberg [50] is shown in figure 5.6, and the difference between undoped and Ln-doped $BiFeO_3$ is apparent. The bulk values are reduced from 0.39 Å to 0.28 for lanthanum, and to 0.288 for samarium. The differences between the two lanthanoids are minute, and the missing $6s^2$ might be an explanation to why the displacement is observed in both compared to undoped $BiFeO_3$.

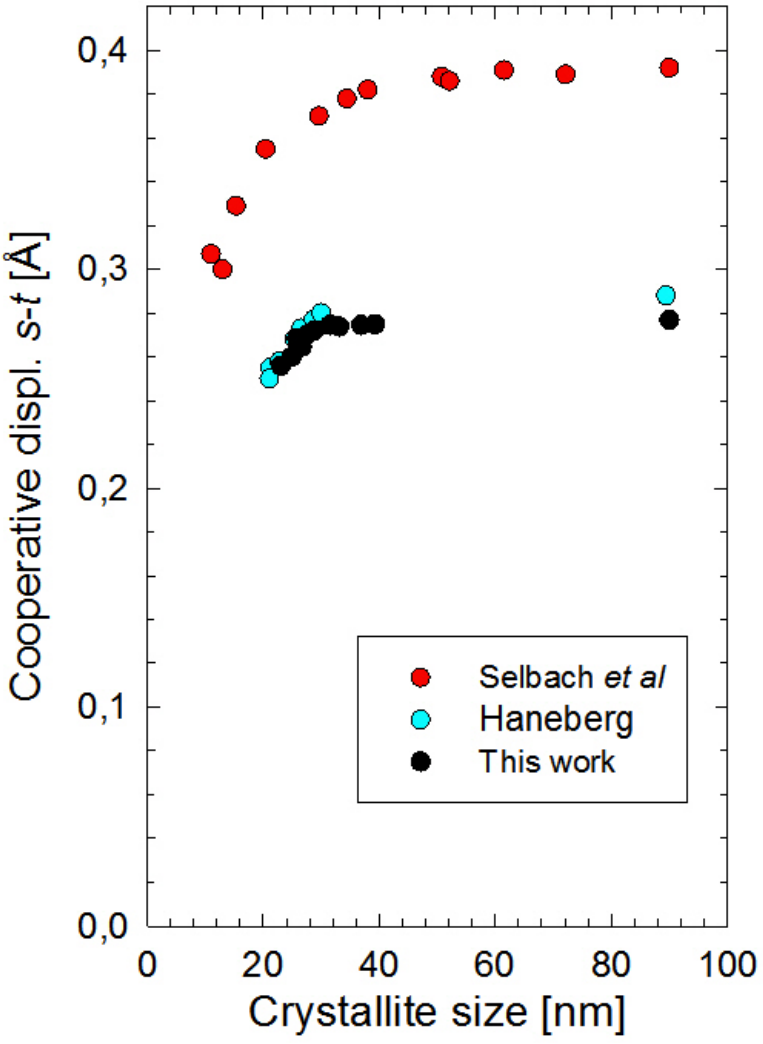

Figure 5.6: The cooperative displacement of Bi^{3+}/La^{3+} and Fe^{3+}, s - t, as a function of the crystallite size for: (red) Selbach *et al.* [5]; (cyan) Haneberg [50]; (black) this work. Both Ln-substituted compositions show a similar size-dependence of the displacement as $BiFeO_3$, although the contribution is smaller.

5.2.4 Size effects

From figures 5.3, 5.4 and 5.5 it seems that the perovskite structure of $Bi_{0.9}La_{0.1}FeO_3$ is able to maintain its lattice parameters even down to relative small crystallites (∼30 nm). Comparing this data with earlier experiments on undoped $BiFeO_3$ reveal much of the same properties found in this work.

There are, however, some important differences when introducing lanthanum to the perovskite structure of $BiFeO_3$. Comparing the lattice parameters of La-doped $BiFeO_3$ with the undoped structure in Selbach [5], it is clear that while the lattice parameter a is shown to be an almost exact match compared to the undoped $BiFeO_3$, the c-parameter is lower over the entire measured range. This is explained in theory [2] as caused by the $6s^2$ lone pair in Bi^{3+}. The polarization in $BiFeO_3$ is mainly due to this pair along the $[001]_{hex}$ direction, c-axis, and replacing Bi^{3+} for La^{3+} will reduce c while a remains fixed. As the bonding between La^{3+} and O^{2-} is mainly ionic, the small covalent nature of the bonding between Bi^{3+} and O^{2-} contributes to this effect [67]. This also explains the relatively lower pseudotetragonality as well as the lower unit cell volume, as they are calculated from both parameters.

5.3 Thermal analysis

In this work, both differential scanning calorimetry (DSC) and differential thermal analysis (DTA) were performed on a selection of samples to observe any effects on phase transitions due to crystallite size. The difference between the two techniques are sensitivity and temperature range; DSC has a higher sensitivity over a smaller range of temperature with a maximum of 550°C, while DTA spans over a wider range with a maximum temperature above 850°C. As theory predicts T_N to be below 400°C and T_C above 600°C, DSC was used to observe the former while DTA the latter.

As the phase transitions are sensitive to the heating/cooling rate, all heat flow measurements were done while both being heated and cooled at 40°C/min for all samples.

5.3.1 Néel temperature

Figure 4.5 shows the DSC data of the selected samples during both heating and cooling and gives the heat flow as a function of temperature. As the crystallite size is reduced, the cusps in the plots are becoming more diffuse due to the change in thermal energy introduced to the structure from reduced calcining temperature. This makes it hard to specify exactly where the antiferromagnetic to paramagnetic transition occurs; the Néel temperature.

From figure 4.5c a clear size-dependency is visible, both for heating and cooling, with a bulk value of ∼393°C and ∼378°C, respectively. The smallest crystallite to show any phase transition was ∼25 nm, occurring at ∼379°C and ∼365°C. Figure 5.7 compares the heating and cooling value of the data from this work with $Bi_{0.9}La_{0.1}FeO_3$ (Hatling [24]), $Bi_{0.9}Sm_{0.1}FeO_3$ (Haneberg [50]) and $BiFeO_3$ (Selbach [5]), and the same trends can be found. For the structures doped with lanthanum or samarium, the phase transition is seen to occur at a higher temperature than for the undoped structure ($T_{N,La} > T_{N,Sm} > T_{N,undoped}$).

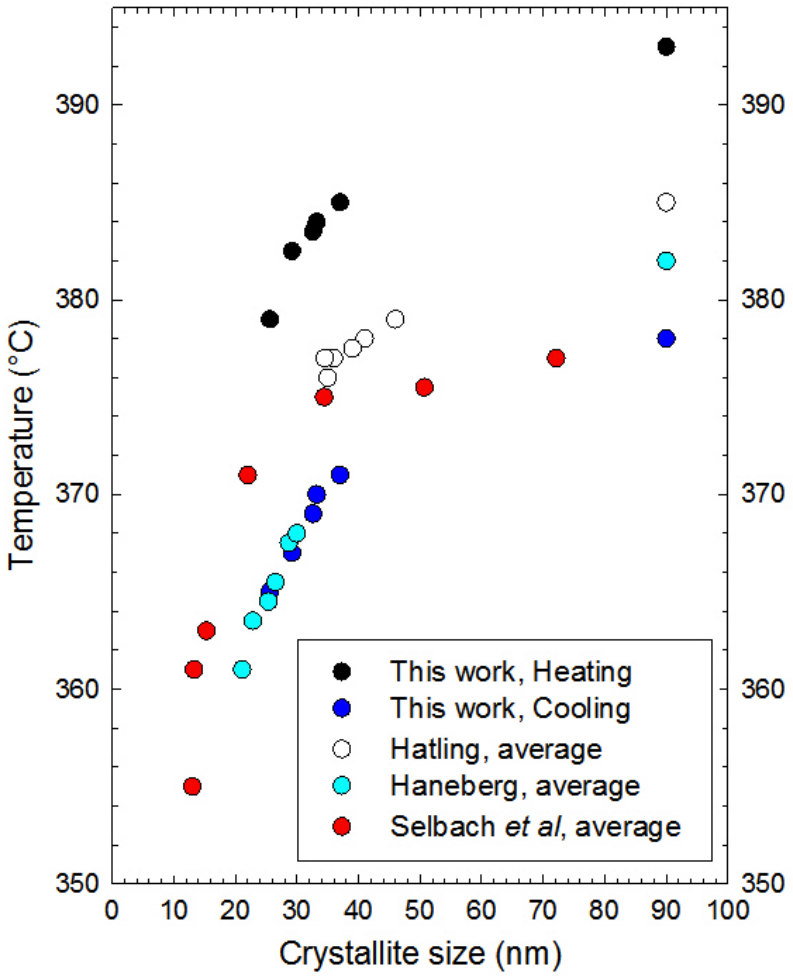

Figure 5.7: The Néel temperature measured in air with a heating rate of 40°/min as a function of crystallite size for: (black) this work, heating; (blue) this work, cooling; (white) Hatling, average [24]; (cyan) Haneberg, average [50]; (red) Selbach *et al.*, heating [5]. The Ln-substituted compositions show a higher average Néel temperature than pure $BiFeO_3$.

As seen from table 2.5 the measured value for $Bi_{0.9}La_{0.1}FeO_3$ in this work is as expected, with an average of the temperature from heating and cooling at ∼385°C for bulk sized crystallites.

5.3.2 Curie temperature

As figure 2.9 shows, the Curie temperature T_C of $BiFeO_3$, separating the ferroelectric phase from the paraelectric one, changes as to what rare earth metal dopant is used. As lanthanum is the left-most lanthanoid in the periodic table, making it the largest by size, a higher Curie temperature is to be expected compared to other rare earth metals such as samarium or gadolinium [48]. The effect of Ln-substitution of $BiFeO_3$ comes from the reduced distortion of the unit cell. Figure 4.6a gives the heat flow as a function of temperature in the range where the phase transition is expected to occur measured by differential thermal analysis (DTA). The first order phase transitions were determined

as the onset of the thermal events, and for the top most plot representing bulk values this was measured to ∼670°C. As explained in chapter 2.1.1 and shown in figures 2.2 and 4.2, an increase in temperature causes the crystallites to grow. As the temperatures in which the DTA was performed surpassed the calcining temperature for all samples, the crystallite growth, thus also the crystallite size, was difficult to measure exactly. To reduce this effect the analysis was performed at a heat rate of 40°C/min. As figure 4.6b shows, most of the samples show signs of further crystallization at temperatures above their T_C, increasing their size.

Comparing the onset of the peak around 680°C for the samples, a difference can be observed between them (see figure 5.8). The onset for the samples from synthesis 1 is measured at ∼660°C, while that from synthesis 2 is measured at ∼640°C.

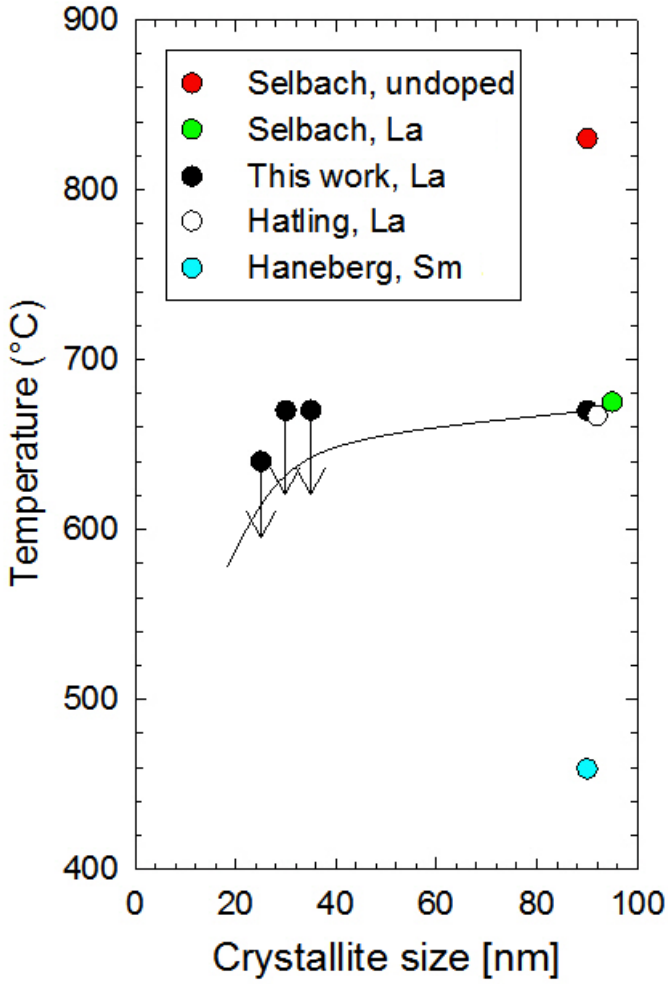

Figure 5.8: Curie temperature measured in air with a heating rate of 40°/min as a function of crystallite size for: (red) Selbach *et al.* [2]; (green) Selbach [5]; (black) this work, (white) Hatling [24]; (cyan) Haneberg [50]. Bulk values as expected from theory, with Sm and La substituted compositions at a lower temperature. Arrows marks the qualitatively potential measurement error due to crystallite growth, and full line acts as a guide to the eye.

As no exact measure of the crystallite size is available throughout the analysis, these are maximum values for crystallites at the given sizes and arrows show the qualitatively errors. One could expect these values to be considerable less if the assumed crystallite growth was not occurring during the thermal analysis.

Selbach [2] and Haneberg [50] observed the same effect when measuring the size-dependent ferroelectric Curie temperature. No measurements of T_C were accessible as rapid particle coarsening occurred upon heating before T_C was reached.

5.4 Finite size effects

It is clear that $Bi_{0.9}La_{0.1}FeO_3$ experience size dependent properties, seen from the data on pseudotetragonality (figure 4.3), the cooperative cationic displacement (4.4), Néel temperature (figure 4.5) and the Curie temperature (figure 5.8). But the point in which this dependence is evident is not exactly the same for all measurements.

Figure 5.9a shows the pseudotetragonality as a function of the cooperative displacement, *s* - *t*, and this is shown not to be linear indicating a more complex interaction than linear displacement of cations with reduced lattice parameters. From this data, the cations displace before the lattice does.

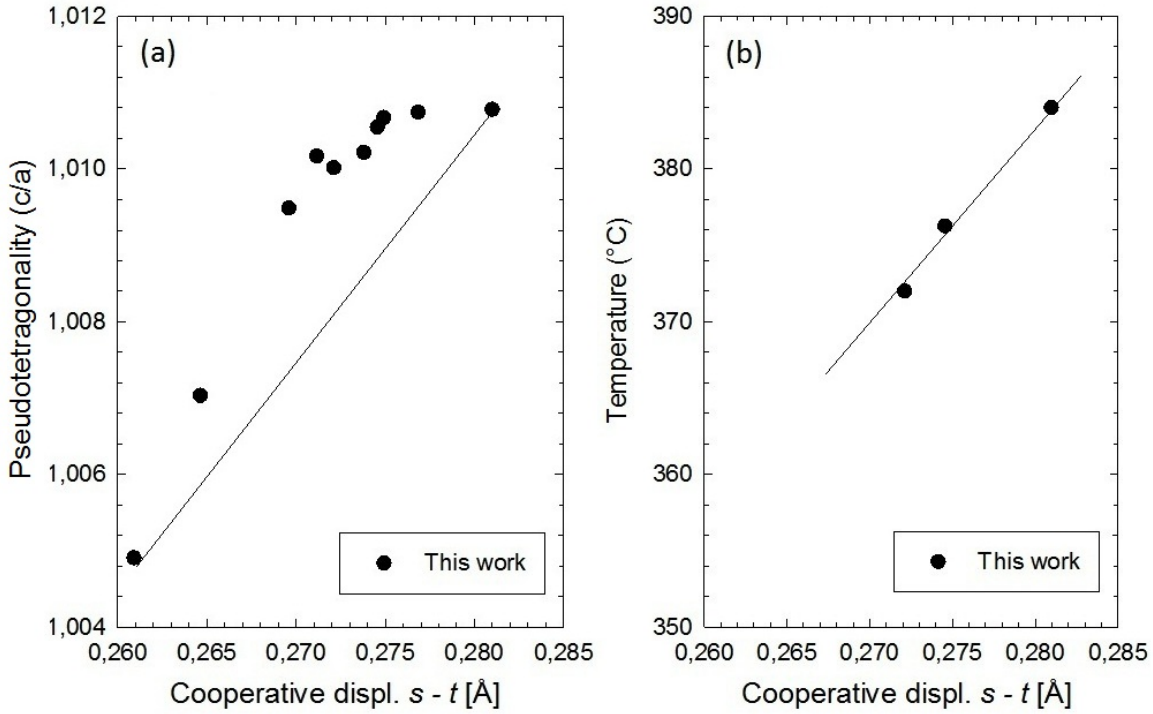

Figure 5.9: (a) Pseudotetragonality and (b) Néel temperature as a function of the cooperative displacement of Bi^{3+}/La^{3+} and Fe^{3+}, *s* - *t*. The latter (b) shows a linear relationship with the displacement, while the former (a) deviates from this linear dependence indicating a more complex interaction than the latter. The solid black line acts as a linear guide for the eye in both figures.

An indication of the critical size for the pseudotetragonality lattice to reach unity can be made by extrapolation of the data in figure 4.3. This was shown to be 15 nm, 6 nm larger than that of undoped $BiFeO_3$ shown in Selbach [5].

Figure 5.9b compares T_N and s - t for the same crystallite size, and a linear dependence is shown. The decrease in T_N could be associated with the decrease in spontaneous polarization quantified by s - t, in addition to the decrease in number of antiferromagnetic interactions with decreasing particle volume. A similar linear dependence between the two parameters was shown by Selbach [5] for undoped $BiFeO_3$.

When comparing the data on $Bi_{0.9}La_{0.1}FeO_3$ with that of $Bi_{0.9}Sm_{0.1}FeO_3$ done in [50] it is clear that the size effects are quite similar. Most of the effects shown are due to the loss of $6s^2$ lone pairs of Bi^{3+} by the Ln doping, but some of the data is shown to be more complex.

6 Conclusion

This work has focused on the synthesis of $BiFeO_3$ doped with 10 at% lanthanum using a modified Pechini wet chemical method. Calcination of green body powder, X-ray diffraction of crystallites of different sizes, calculation of lattice parameters and cationic displacements as well as thermal analysis to determine phase transition temperatures has been performed and compared with literature.

The synthesis modification of adding 10 at% lanthanum at the expense of bismuth has been shown by XRD to work out well. Small amounts of secondary phases has been shown to occur at small crystallite sizes, but not to the extent that it interfered with the qualitatively measurements. The deviation from $BiFeO_3$ is observable by most characterization methods, and a size-dependency measured by the pseudotetragonality is shown to occur for crystallites smaller than ∼30 nm. The average Néel temperature was shown to decrease from 385°C for bulk sized crystallites to 372°C at 26 nm, and the Curie temperature, although hard to quantify, showed some size-dependent properties being reduced from 670°C to 640°C. Displacement of the cations was shown to be smaller than that of $BiFeO_3$ and of the same magnitude as $BiFeO_3$ doped with samarium. The displacement was seen before the reduced pseudotetragonality occurred, indicating a more complex nature of the properties other than reduced lattice parameters.

Based on these results, it seems that the crystallite size dependency of the perovskite lattice parameters, a and c, observed in $BiFeO_3$ is also present in $Bi_{0.9}La_{0.1}FeO_3$. In the former, the size dependency is thought to come from the scaling relation and possible correlations with the decreasing polarization in the $[001]_{\text{hex}}$ direction. This work has shown a decrease in this direction due to the removal of the $6s^2$ lone pairs of Bi^{3+} at the expense of added La^{3+}-ions.

To fully understand the nature of the size-dependent properties of $Bi_{0.9}La_{0.1}FeO_3$, a comprehensive magnetic characterization to examine the antiferromagnetic properties is needed.

References

[1] G. A. Smolenskiĭ, I. E. Chupis, *Ferroelectromagnets*, Sov. Phys. Usp. (1982), Vol. 25, pp. 475-493.

[2] S. M. Selbach, *Structure, stability and phase transitions of multiferroic $BiFeO_3$*, Doctoral thesis at NTNU (2009).

[3] F. G. Garcia, C. S. Riccardi, A. Z. Simões, *Review: Lanthanum doped $BiFeO_3$ powders: Syntheses and characterization*, Journal of Alloys and Compounds (2010), Vol. 501, pp. 25 - 29.

[4] D. Khomskii, *Classifying multiferroics: Mechanisms and effects*, Physics (2009), Vol. 2

[5] S. M. Selbach, T. Tybell, M-A. Einarsrud, T. Grande, *Size-dependent properties of multiferroic* $BiFeO_3$ *nanoparticles*, Chem. Mater (2007), Vol. 19, pp 6478 - 6484

[6] M. Tanakaab, Y. Makinoac, Finite size effects in submicron barium titanate particles, Ferroelectrics Letters Section (1998), Vol. 24, pp 13 - 23

[7] L. Sun, P. C. Searson, C. L. Chien, *Finite-size effects in nickel nanowire arrays*, Physical Review B (2000), Vol. 61, pp 6463 - 6466

[8] K. R. Xhu, M. S. Zhang, Y. Dheng, J. X. Zhou, Z. Yin, *Finite-size effects of lattice structure and soft mode in bismuth titanate nanocrystals*, Solid State Communications (2008), Vol. 145, pp 456 - 560

[9] I. Sosnowska, T-P. Neumaier, E. Steichele, *Spiral magnetic ordering in bismuth ferrite*, J. Phys. C: Solid State Phys. (1982), Vol. 15, pp 4835 - 4846

[10] G. Le Bras, P. Bonville, D. Colson, A. Forget, N. Genand-Riondet, R. Tourbot, *Effect of La doping in the multiferroic compound $BiFeO_3$*, Physica B (2011), Vol. 406, pp 1492–1495

[11] A. A. Amirov, I. K. Kamilov, A. B. Batdalov, I. A. Verbenko, O. N. Razumovskaya, L. A. Reznichenko, L. A. Shilkina, *Magnetoelectric interactions in $BiFeO_3$, $Bi_{0.95}Nd_{0.05}FeO_3$ and $Bi_{0.95}La_{0.05}FeO_3$ multiferroics*, Tech. Phys. Lett. (2008), Vol. 34, pp 760 - 762.

[12] J. Wei a, D. Xuea, C. Wu, Z. Li, *Enhanced ferromagnetic properties of multiferroic $Bi_{1-x}Sr_xMn_{0.2}Fe_{0.8}O_3$ synthesized by sol–gel process*, J. All. Com. (2008), Vol. 453, pp 20 - 23

[13] I. Sosnowska, W. Schäfer, W. Kockelmann, K. H. Andersen, I. O. Troyanchuk, *Crystal structure and spiralmagnetic ordering of $BiFeO_3$ doped with manganese*, Appl. Phys. A (2002), Vol. 74, pp S1040 - S1042

[14] X. Yan, J. Chen, Y. Qi, J. Cheng, Z. Meng, *Hydrothermal synthesis and characterization of multiferroic* $Bi_{1-x}La_xFeO_3$ *crystallites*, J. Eur. Cer. Soc. (2010), Vol. 30, pp 265 - 269

[15] Y-H. Lin, Q. Jiang, Y. Wang, C-W. Nan, *Enhancement of ferromagnetic properties in* $BiFeO_3$ *polycrystalline ceramic by La doping*, Appl. Phys. Let. (2007), Vol. 90, pp 172507-1/3

[16] A. Z. Simões, E. C. Aguiar, A. H. M. Gonzalez, J. Andrés, E. Longo, J. A. Varela, *Strain behavior of lanthanum modified* $BiFeO_3$ *thin films prepared via soft chemical method*, J. Appl. Phys. (2008), Vol. 104, 104115

[17] M. Bibes, A. Barthélémy, *Towards a magnetoelectric memory*, Nature Mater. (2008), Vol. 7, pp 425 - 426

[18] Y-H. Chu, L. W. Martin, M. B. Holocomb, M. Gajek, S-J. Han, Q. He, N. Balke, C-H. Yang, D. Lee, W. Hu, Q. Zhan, P-L. Yang, A. Fraile-Rodriguez, A. Scholl, S. X. Wang, R. Ramesh, *Electric-field control of local ferromagnetism using a magnetoelectric multiferroic*, Nature Mater. (2008), Vol. 7, 478 - 482

[19] C. J. Brinker, *Sol-gel science: The physics and chemistry of sol-gel processing*, Academic Press Inc. 1990

[20] A. C. Pierre, *Introduction to sol-gel processing*, Kluwer Academic Publishers 1998, USA

[21] C. Kumar, *Nanostructured oxides*, Wiley-VCH 2009, Germany

[22] PM. P. Pechini, U.S. Patent 3,330,697 (July 11, 1967)

[23] C. Lin, C. Zhang, J. Lin, *Phase transformation and photoluminescence properties of nanocrystalline ZnO2 powders prepared via the Pecchini-type sol-gel process*, J. Phys. Chem. C (2007), Vol. 111, pp 3300 - 3307

[24] O. Hatling, *Multiferroic, magnetoelectric nanoparticles: Lanthanum-substituted Bismuth Ferrite*, Project course report at NTNU (2010).

[25] A. R. West, *Basic solid state chemistry*, Wiley, 2nd Edition 2002, England

[26] M. T. Dove, *Structure and dynamics: An atomic view of materials*, Oxford University Press, 1st Edition 2003, USA

[27] V. M. Goldschmidt, *Die Gesetze der Krystallochemie*, Naturwissenschaften, Vol. 14, pp. 477-485

[28] D. W. Richerson, *Modern Ceramic Engineering: Properties, processing and use in design*, Taylor & Francis Group, 3rd Edition 2006, USA

[29] K. M. Rabe, C. H. Ahn, J-M. Triscone, *Physics of ferroelectrics: A modern perspective*, Springer-Verlag Berlin Heidelberg 2007

[30] J. M. Moreay, C. Michel, R. Gerson, W. J. James, *Ferroelectric* $BiFeO_3$ *X-ray and neutron diffraction study*, J. Phys. Chem. Solids (1971), Vol. 32, pp 1315 - 1320

[31] F. Kubel, H. Schmid, *Structure of a ferroelectric and ferroelastic monodomain crystal of the perovskite bismuth iron oxide* $BiFeO_3$, Acta Cryst. (1990), Vol. 46, pp 698 - 702

[32] H. D. Megaw, C. N. W. Darlington, *Geometrical and structural relations in the rhombohedral perovskites*, Acta Cryst. (1975). Vol. A31, pp. 161 - 173

[33] K. Ishikawa, T. Uemori, *Surface relaxation in ferroelectric perovskites,* Phys. Rev. B (1999), Vol. 60, pp 11841 - 11845

[34] T. T. Carvalho, P. B. Tavares, *Synthesis and thermodynamic stability of multiferroic $BiFeO_3$*, Materials Letters (2008), Vol. 62, pp 3984 – 3986

[35] M. Popa, D. Crespo, J. M. Calderon-Moreno, *Synthesis and Structural Characterization of Single-Phase $BiFeO_3$ Powders from a Polymeric Precursor*, J. Am. Ceram. Soc. (2007), Vol. 90 , pp 2723 – 2727

[36] S, Ghosh, S. Dasgupta, A. Sen, H. M. Maiti, *Low-temperature synthesis of nanosized bismuth ferrite by soft chemical route*, J. Am. Ceram. Soc. (2005), Vol. 88, pp 1349 - 1352

[37] D. Lebeugle, D. Colson, A. Forget, M. Viret, P. Bonville, J. F. Marucco, S. Fusil, *Room-temperature coexistence of large electric polarization and magnetic order in $BiFeO_3$ single crystals*, Physical Review (2007), Vol. 76, pp 024116-1/8

[38] Q-H. Jiang, C-W. Nan, Y. Wang, Y-H. Liu, Z-J. Shen, *Synthesis and properties of multiferroic $BiFeO_3$ ceramics*, J. Electroceram (2008), Vol. 21, pp 690 - 693

[39] G. Catalan, J. F. Scott, *Physics and Applications of Bismuth Ferrite*, Adv. Mater. (2009), Vol. 21, 2463 - 2485

[40] R. D. Shannon, *Revised Effective Ionic-Radii and Systematic Studies of Interatomic Distances in Halides and Chalcogenides*, Acta Crystallogr. (1976), Vol. A32, pp 751 - 767

[41] S. R. Das, R. N. P. Choudhary, P. Bhattacharya, R. S. Katiyar, P. Dutta, A. Manivannan, M. S. Seehra, *Structural and multiferroic properties of La-modified $BiFeO_3$ ceramics,* J. Appl. Phys. (2007), Vol. 101, pp 034104-1/7

[42] M. Fiebig, V. V. Eremenko, I. E. Chupis, *Magnetoelectric interaction phenomena in crystals*, Kluwer Academic Publishers 2003, The Netherlands

[43] R. E. Cohen, *Origin of Ferroelectricity in Perovskite Oxides*, Nature (1992), Vol. 358, pp 136 - 138

[44] Y. Kuroiwa, S. Aoyagi, A. Sawada, J. Harada, E. Nishibori, M. Takata and M. Sakata, *Evidence for Pb-O covalency in tetragonal $PbTiO_3$*, Phys. Rev. Lett. (2001), Vol. 87, pp 217601

[45] J. B. Neaton, C. Ederer, U. V. Waghmare, N. A. Spaldin, K. M. Rabe, *First-principles study of spontaneous polarization in multiferroic $BiFeO_3$*, Phys. Rev. B (2005), Vol. 71, pp 014113

[46] P. Ravindran, R. Vidya, A. Kjekshus, H. Fjellvåg, O. Eriksson, *Theoretical investigation of magnetoelectric behavior in $BiFeO_3$,* Physical Review B (2006), Vol. 74, pp 224412 - 1/18

[47] M. M. Kumar, V. R. Palkar, K. Srinivas and S. V. Suryanarayana, *Ferroelectricity in a pure $BiFeO_3$ ceramic*, Appl. Phys. Lett. (2000), Vol. 76, pp 2764 - 2766

[48] S. Karimi, I. M. Reaney, Y. Han, J. Pokorny, I. Sterianou, *Crystal chemistry and domain structure of rare-earth doped* $BiFeO_3$ ceramics, J. Mater. Sci. (2009), Vol. 44, pp 5102 - 5112

[49] H. Uchida, R. Ueno, H. Funakubo, S. Koda, *Crystal structure and ferroelectric properties of rare-earth substituted $BiFeO_3$ thin films*, J. App Phys. (2006), Vol. 100, pp 014106 1/9

[50] D. H. A. Haneberg, *A finite size study on samarium substituted bismuth ferrite multiferroic and lead-free piezoelectric materials*, Master report at NTNU (2010).

[51] J. R. Cheng, R. Eitel, L. E. Cross, *Lanthanum-modified (1-x)$(Bi_{0.8}La_{0.2})(Ga_{0.05}Fe_{0.9})O_3$·x$PbTiO_3$ crystalline solutions: Novel morphotropic phase-boundary lead-reduced piezoelectrics*, JACerS (2003), Vol. 86, pp 2111–2115

[52] J. B. Goodenough, *Theory of the Role of Covalency in the Perovskite-Type Manganites [La,M(II)]MnO_3*, Phys. Rev. (1955), Vol. 100, pp 564-573

[53] A. Manzoor, S. K. Hasanain, *Size effects on multiferroic behavior of $BiFeO_3$ nanoparticles*, Retrieved (2010, December 13) from http://www.ncp.edu.pk/docs/iss/talks/Group%202/Day-4/Alina_manzoor_Ferroelectric_and_Ferromagnetic_behaviour_of_BiFeO3.pdf

[54] W. C. Koehler, E. O. Wollan, M. K. Wilkinson, *Neutron diffraction study of the magnetic properties of rare-earth-iron perovskites*, Phys. Rev. (1960), Vol. 118, pp 58 - 70.

[55] J. R. Chena, W. L. Wangb, J. B. Lia, G. H. Raoa, *X-ray diffraction analysis and specific heat capacity of $Bi_{1-x}La_xFeO_3$ perovskites*, Journal of Alloys and Compounds (2008), Vol. 459, pp 66 - 70

[56] Y. Ivry, *Ferroelectricity and Ferroelasticity at the Nanoscale*, Retrieved (2010, December 14) from http://www.phys.huji.ac.il/Lectures/Ivri_Abstract.pdf

[57] W. Eerenstein, N. D. Mathur, J. F. Scott, *Review: Multiferroic and magnetoelectric materials*, Nature (2006), Vol. 442, pp 759 - 765

[58] S-W. Cheong, M. Mostovoy, *Multiferroics: a magnetic twist for ferroelectricity*, Nature Materials (2007), Vol. 6, pp 13 - 20

[59] R. Ramesh, N. A. Spaldin, *Multiferroics: progress and prospects in thin films*, Nature Materials (2007), Vol. 6, pp 21 - 29

[60] R. Seshadri, N. A. Hill, *Visualizing the role of Bi 6s "lone pairs" in the off-center distortion in ferromagnetic $BiMnO_3$*. Chem. Mater. (2001), Vol. 13, pp 2892 - 2899

[61] X. G. Zheng, C. N. Xu, K. Nishikubo, K. Nishiyama, W. Higemoto, W. J. Moon, E. Tanaka, E. S. Otabe, *Finite-size effect on Néel temperature in antiferromagnetic nanoparticles*, Phys. Rev. B (2005), Vol. 72, 014464 1/8

[62] M-S Zhang, Z. Yina, Q. Chena, W. Zhangb, W. Chenc, *Study of structural and photoluminescent properties in barium titanate nanocrystals synthesized by hydrothermal process*, Solid State Communications (2001), Vol. 119, pp 659 - 663

[63] V. R. Palkar, J. John, R. Pinto, *Observation of saturated polarization and dielectric anomaly in magnetoelectric $BiFeO_3$ thin films*, Appl. Phys. Lett. (2002), Vol. 80, pp 1628 - 1630

[64] H. M. Rietveld, *A Profile Refinement Method for Nuclear and Magnetic Structures*, J. Appl. Crystallogr., (1969), Vol. 2, pp 65

[64] T-J. Park, G. C. Papaefthymiou, A. J. Viescas, A. R. Moodenbaugh, S. S. Wong, *Size-dependent Magnetic properties of single-crystalline multiferroic $BiFeO_3$ nanoparticles*, Nano Letter (2007), Vol. 7, pp. 766 - 772.

[65] A. L. Patterson, *The Scherrer Formula for X-Ray Particle Size Determination*, Phys. Rev. (1939), Vol. 56, pp 978 – 982

[66] P. Ayyub, V. R. Palkar, S. Chattopadhyay, M. Multani, *Effect of crystal size-reduction on lattice symmetry and cooperative properties*, Phys. Rev B (1995), Vol. 51, pp 6135 - 6138

[67] R. Sæterli, S. M. Selbach, P. Ravindran, T. Grande, R. Holmestad, *Electronic structure of multiferroic $BiFeO_3$ and related compounds: Electron energy loss spectroscopy and density functional study*, Phys. Rev. B. (2010), Vol. 82, pp 064102 1/9